Sparsity-Based Time-Frequency Representation of FM Signals with Burst Missing Samples

Vaishali S. Amin, Yimin D. Zhang, and Braham Himed

Abstract

In this paper, we present an effective time-frequency (TF) analysis of non-stationary frequency modulated (FM) signals in the presence of burst missing data samples. The key concept of the proposed work lies in the reliable sparse recovery of non-parametric FM signals in the joint-variable domains. Specifically, by utilizing the one-dimensional Fourier relationship between the instantaneous auto-correlation function (IAF) and the TF representation (TFR), the proposed approach iteratively recovers missing samples in the IAF domain through sparse reconstruction using, e.g., the orthogonal matching pursuit (OMP) method, while maintaining the TF-domain sparsity. The proposed method, referred to as missing data iterative sparse reconstruction (MI-SR), achieves reliable TFR recovery from the observed data with a high proportion of burst missing samples. This is in contrast to the existing sparse TFR recovery methods which work well only for random missing data samples. In particular, when applied in conjunction with signal-adaptive TF kernels, the proposed method achieves effective suppression of both cross-terms and artifacts due to burst missing samples. The superiority of the proposed technique is verified through analytical results and numerical examples.

Index Terms

Burst missing sample, compressive sensing, non-stationary signal, sparse reconstruction, time-frequency representation.

The work of V. S. Amin and Y. D. Zhang is supported in part by a subcontract with Matrix Research, Inc. for research sponsored by the Air Force Research Laboratory under contract FA8650-14-D-1722.

V. S. Amin and Y. D. Zhang are with the Department of Electrical and Computer Engineering, Temple University, Philadelphia, PA, 19122, USA (e-mail: vamin@temple.edu; ydzhang@temple.edu).

B. Himed is with the Air Force Research Laboratory, AFRL/RYMD, Dayton, OH 45433, USA.

I. Introduction

Many practical signals are non-stationary in nature. An important class of non-stationary signals is the frequency-modulated (FM) signal that is characterized by their time-varying instantaneous frequencies (IFs). FM signals are found in a wide spectrum of applications in the areas of seismic, radar, sonar, wireless communications, image processing, speech processing, and biomedical applications [1]–[4]. The time-frequency representations (TFRs) of FM signals bear significant practical importance. For example, in the field of radar signal processing, time-frequency (TF) analyses and IF estimation are crucial for various important applications, such as target detection and tracking [5]–[9]. In recent decades, TF analyses have received considerable research interests for the characterization, parameter estimation, and IF estimation of various non-stationary signals [10]–[16]. In this paper, we focus our discussion on the quadratic TFRs.

In practice, the problem of missing data samples is commonly encountered in many real-world signal processing applications due to sensor failure, removal of noisy and jammed measurements, line-of-sight obstruction, destructive multipath fading, and logistics in data sampling and storage [17]. A number of publications have addressed the TF analysis in the presence of random missing samples [18]–[24]. Generally, these approaches are developed based on leveraging compressive sensing (CS) techniques by exploiting the sparsity of the signals in the TF domain [25]. The proper use of TF kernels, which are originally developed for cross-term reduction, also mitigates the effect of artifacts due to missing samples [18]. In general, adaptive (data-dependent) TF kernels, such as the commonly used adaptive optimal kernel (AOK) [26], [27] and the recently developed adaptive directional TF distribution (ADTFD) [28], generally outperform fixed (data-independent) TF kernels in terms of cross-term mitigation, while preserving high energy auto-term signal signatures. CS-based TFR reconstruction has successfully found applications in, e.g., radar, communications, direction finding, satellite navigation, and observational astronomy [29]–[39].

Compared to the random missing sample case, a more realistic and challenging scenario is that the data contains burst missing samples, i.e., the missing samples are clustered as consecutive bursts. Such burst missing samples may be observed, for example, in the above mentioned interrupting examples where the interference or fading lasts much longer than the sampling interval. It is clear that, compared with the case with random missing samples, such burst missing samples would make the TF analysis and IF estimation much more difficult. As we will see, unlike the random missing sample case where the artifacts due to missing samples are uniformly distributed in the TF domain, burst missing samples cause artifacts that are highly localized around the true IF signatures, obscuring the identification of true signal IF signatures. Burst missing samples also make signal filtering and interpolation less effective.

In [40], resilient TF analysis of non-stationary FM signals in the presence of burst missing samples is

considered. In this method, the missing data iterative adaptive approach (MIAA) [41] is used to iteratively compute the TFR of the FM signals from the instantaneous auto-correlation function (IAF) with missing entries due to the burst missing samples. The MIAA was originally developed for the recovery of stationary signals with random or burst missing data [41] and works on the principle of sequential estimation of the Capon spectrum estimator and missing data recovery through data interpolation/extrapolation. As the MIAA is designed for stationary signals, it does not work properly when it is directly applied to non-stationary FM signals with burst missing data. However, the IAF of non-stationary FM signals is stationary with respect to the lag and is associated with the TFR through a one-dimensional (1-D) Fourier transform with respect to the lag. As such, the MIAA is found effective in reconstructing the TFR as well as filling in the missing IAF entries in the time-lag domain [40].

In this paper, we further extend this study and aim to provide a comprehensive analysis of TFR reconstruction in the presence of burst missing samples under the sparse reconstruction framework. We first examine the effects of burst missing data on the IAF, ambiguity function (AF), and TFR. We then develop a non-parametric iterative CS-based algorithm, referred to as the missing data iterative sparse reconstruction (MI-SR), for reliable TFR reconstruction of FM signals in such situations. Our main motivation behind this novel algorithm lies in the fact that, usually, FM signals are sparsely represented in the TF domain. In this scenario, various CS-based techniques, which exploit the signal sparsity, can be used for TFR reconstruction. Amongst various compressive sensing based approaches, we choose the orthogonal matching pursuit (OMP) in this paper for its simplicity [42]. Other CS techniques, such as LASSO and Bayesian CS [43]–[47], can also be used in lieu of the OMP technique.

The proposed MI-SR iteratively updates the missing information through spectral estimation obtained during subsequent iterations. By utilizing the 1-D Fourier transform that relates the IAF and the TFR, rather than the two-dimensional (2-D) Fourier transform relationship between the ambiguity and TF domains as in [25], [48], the proposed MI-SR technique presents significantly lower complexity and better control of the spectrum sparsity over each time instant. The effectiveness of the proposed algorithm is verified by comparing it with the kernel-based approach [18] and the MIAA-based approach [40]. The analytical and numerical results provided in this paper clearly demonstrate the superiority of the proposed MI-SR technique over these methods in terms of the TFR reconstruction performance, artifact suppression capability, and reduced computational complexity, mainly benefited from the effective utilization of the high sparsity of the FM signals. The proposed MI-SR method can also be applied to kerneled IAF for further cross-term reduction and performance improvement.

The remainder of the paper is organized as follows. We provide the signal model in Section II and consider a detailed analysis of the effects of burst missing data samples on the IAF, AF, and TFR

domains along with demonstration examples in Section III. The proposed MI-SR algorithm for sparse signal recovery is derived in Section IV, followed by simulation results in Section V. Finally, concluding remarks are provided in Section VI.

Notations. A lower (upper) case bold letter represents a vector (matrix). $(\cdot)^*$, $(\cdot)^T$, and $(\cdot)^H$, respectively, stand for complex conjugation, transpose, and conjugate transpose (Hermitian). $\mathcal{F}_s(\cdot)$ and $\mathcal{F}_s^{-1}(\cdot)$ respectively express the discrete Fourier transform (DFT) and inverse DFT (IDFT) with respect to s. $||\cdot||_0$ and $||\cdot||_2$ respectively denote the ℓ_0-norm and ℓ_2-norm of a vector. In addition, $\delta(t)$ and $\delta(t,\tau)$ respectively denote 1-D and 2-D Kronecker delta functions.

II. Signal Model and Joint-Variable Domain Representations

A. Signal Model

Consider a discrete-time signal, $s(t), t = 1, ..., T$, which consists of a single or multiple non-stationary FM signal components. The observed signal, denoted as $r(t)$, contains a total number of B bursts of missing samples. The missing sample bursts are randomly distributed over time and are assumed to be mutually non-overlapping. Denote N_b as the number of missing samples in the bth burst for $b = 1, 2, ..., B$. The total number of missing samples is $N = \sum_{b=1}^{B} N_b$, with $0 \leq N < T$.

Denote $\mathbb{S} \subset \{1, ..., T\}$ as the set of observed time instants with a cardinality of $|\mathbb{S}| = T - N$. Similarly, we define the set of missing entries related to the bth burst as $\bar{\mathbb{S}}_b = \{t_{b1}, ..., t_{bN_b}\}$ for $b = 1, 2, ..., B$, and denote $\bar{\mathbb{S}} = \bigcup_{b=1}^{B} \bar{\mathbb{S}}_b$ as the complete set of missing samples with $|\bar{\mathbb{S}}| = N$. Then, the observed signal, $r(t)$, can be expressed as the product of $s(t)$ and an observation mask, $R(t)$, i.e.,

$$r(t) = s(t) \cdot R(t), \tag{1}$$

where

$$R(t) = \begin{cases} 1, & \text{if } t \in \mathbb{S}, \\ 0, & \text{if } t \notin \mathbb{S}. \end{cases} \tag{2}$$

Similarly, the missing data can be expressed as the product of the original signal, $s(t)$, and the missing data mask, $M(t)$, i.e.,

$$m(t) = s(t) \cdot M(t), \tag{3}$$

where the missing data mask is defined as

$$M(t) = S(t) - R(t) \ = \sum_{b=1}^{B} \sum_{n=1}^{N_b} \delta(t - t_{bn}) = \sum_{i=1}^{N} \delta(t - t_i), \quad t_{bn} \in \bar{\mathbb{S}}_b, \quad t_i \in \bar{\mathbb{S}}. \tag{4}$$

The original signal mask, $S(t)$, is an all-pass mask, i.e.,

$$S(t) = 1, \quad \forall t. \tag{5}$$

From (3) and (4), the missing signal is expressed as

$$m(t) = \sum_{b=1}^{B} \sum_{n=1}^{N_b} s(t_{bn}) \delta(t - t_{bn}) = \sum_{i=1}^{N} s(t_i) \delta(t - t_i), \quad t_{bn} \in \bar{\mathbb{S}}_b, \quad t_i \in \bar{\mathbb{S}}. \tag{6}$$

The observed signal can be expressed as the difference between the original signal and the missing samples, i.e.,

$$\begin{aligned} r(t) = s(t) - m(t) &= s(t) - \sum_{b=1}^{B} \sum_{n=1}^{N_b} s(t_{bn}) \delta(t - t_{bn}) \\ &= s(t) - \sum_{i=1}^{N} s(t_i) \delta(t - t_i), \quad t_{bn} \in \bar{\mathbb{S}}_b, \quad t_i \in \bar{\mathbb{S}}. \end{aligned} \tag{7}$$

It should be noted that the random missing sample scenario can be considered as a special case of the underlying burst missing sample scenario with B equal to N and N_b equal to 1 in the above expressions.

B. Joint-Variable Analysis in Different Domains

In addition to the joint TF domain, non-stationary signals can also be represented in other joint-variable domains. The other two commonly used joint-variable domains are the ambiguity domain and the time-lag domain (also referred to as the IAF domain). From the perspective of TF analysis of non-stationary signals with burst missing samples, signal representations in these join-variable domains are effective, attributed to the different features offered by these domains. For example, for each time instant the IAF of a non-stationary FM signal is stationary with respect to the lag. This fact is used to obtain robust TFRs from the IAF through the 1-D Fourier transform or the corresponding sparse reconstruction. On the other hand, TF kernels can be conveniently designed as multiplicative functions in the ambiguity domain, as opposed to a convolutive function in the other domains.

The IAF of $s(t)$ is defined in the time-lag (t-τ) domain in terms of time t and lag τ as

$$R_{ss}(t, \tau) = s\left(t + \tau\right) s^*\left(t - \tau\right). \tag{8}$$

The Wigner-Ville distribution (WVD) is the simplest, yet one of the most popular members of the Cohen's class of bilinear distributions [16]. It can be obtained by taking the 1-D DFT of the IAF, $R_{ss}(t, \tau)$, with respect to τ, and can be expressed as

$$W_{ss}(t, f) = \mathcal{F}_{\tau}[R_{ss}(t, \tau)] = \sum_{\tau} R_{ss}(t, \tau) e^{-\jmath 4\pi f \tau}, \tag{9}$$

where $\jmath = \sqrt{-1}$. Note that, in the above DFT expression, 4π is used instead of 2π because only integer valued lags, τ, are used in (8).

The AF of a signal is a joint representation in the θ-τ domain, where θ is the frequency shift and τ is the lag. The AF is obtained by applying a 1-D DFT to the IAF, $R_{ss}(t,\tau)$, with respect to time t, and can be expressed as

$$A_{ss}(\theta,\tau) = \mathcal{F}_t[R_{ss}(t,\tau)] = \sum_t R_{ss}(t,\tau)e^{-\jmath 2\pi\theta t}. \tag{10}$$

Consequently, the WVD can be interpreted as the 2-D DFT of the corresponding AF of the same signal under consideration.

C. Time-Frequency Kernels

The problem of interfering cross-terms arising in quadratic TFRs is a major drawback that prohibits straightforward interpretation of signal energy distribution. An effective measure for cross-term reduction is to apply TF kernels, which are 2-D multiplicative functions in the ambiguity domain that provide low-pass filtering characteristics. Conventionally, TF kernels are designed to attenuate undesired cross-terms while preserving the signal auto-term components.

The choice of a particular TF kernel function, which identifies the specific TF distribution, depends on the application and the class of the signals under consideration. So far, various data-independent and data-dependent TF kernel designs have been proposed. The Choi-Williams distribution kernel [49], the cone kernel [50], and the Born-Jordan kernel (sinc kernel function) [51] are examples of popular data-independent TF kernels. On the other hand, data-dependent kernels are optimized based on the signal characteristics and have generally shown superiority over data-independent kernels in terms of performance. The AOK is a popular choice of data-dependent kernel and is developed based on a radially Gaussian kernel with an angle-dependent size. The AOK is obtained by solving the following radially Gaussian kernel optimization problem defined in the polar coordinates for each time-localized, short-time ambiguity function (STAF) [27]:

$$\begin{aligned} &\max_{\Psi} \int_0^{2\pi}\int_0^{\infty} |A(\alpha,\varphi)\Psi(\alpha,\varphi)|^2 \alpha \, d\alpha \, d\varphi \\ &\text{subject to} \quad \Psi(\alpha,\varphi) = \exp\Big(-\frac{\alpha^2}{2\sigma^2(\varphi)}\Big), \\ &\text{and} \quad \frac{1}{4\pi^2}\int_0^{2\pi} \sigma^2(\varphi)\, d\varphi \;\le \beta, \end{aligned} \tag{11}$$

where $\beta > 0$ is a trade-off between the auto-component smearing and the cross-component suppression. In the above expressions, $A(\alpha,\varphi)$ is the AF in the polar coordinate, $\Psi(\alpha,\varphi)$ is the kernel function, and $\sigma(\varphi)$ is the *spread function* that controls the spread of the Gaussian at the radial angle φ. The radial angle φ and the radius α are related to lag τ and frequency shift θ as $\varphi = \arctan(\tau/\theta)$ and radius

$\alpha = \sqrt{\theta^2 + \tau^2}$. The time-localized TFR corresponding to each optimized AOK is computed by taking the 2-D FFT of the product of the corresponding STAF and the AOK obtained using (11).

It is demonstrated in [18] that the use of AOK improves the TF recovery in the presence of random missing samples. On the other hand, the artifacts in the ambiguity domain due to random missing samples, particularly those concentrated along the $\tau = 0$ axis, may misguide the TF kernel optimization to favor such artifacts and generate highly distorted TFRs [22]. Such artifacts can be mitigated by attenuating the presence of the AF along the $\tau = 0$ axis. For burst missing samples, as we will see in the following section, the artifacts in the ambiguity domain spread around the auto-terms and thus are much more difficult to suppress. Such fact motivates us to develop other sparse reconstruction based techniques to obtain robust TFRs in the presence of burst missing data samples. Our proposed approach, in which the missing data recovery is performed in the IAF domain, overcomes the limitation of the AOK and provides robust TFR reconstruction.

III. Quadratic Time-Frequency Representations with Burst Missing Samples

A. *Effect of Burst Missing Samples*

Missing signal samples in the time domain produce missing entries in the IAF of the received signal with two diagonal missing lines corresponding to each missing sample, meeting at the temporal position of the missing sample [18]. The TFR and the AF are related to the IAF through a 1-D Fourier transform, hence the random missing entries in the IAF induce undesired noise-like artifacts in both the TFR and the AF.

For burst missing samples, however, the characteristics of the yielding artifacts are different. In the following, we provide detailed mathematical analysis related to the effects of burst missing samples on the entries of the IAF in the time-lag domain.

From (1) and (8), the IAF of $r(t)$ is expressed as the product of the IAF of $s(t)$ and the IAF of the observation mask $R(t)$, i.e.,

$$R_{rr}(t,\tau) = R_{ss}(t,\tau) R_{RR}(t,\tau). \tag{12}$$

In this expression, the IAF of $R(t)$, $R_{RR}(t,\tau)$, is a binary masking function and can be decomposed into the following terms:

$$R_{RR}(t,\tau) = R_{SS}(t,\tau) + R_{MM}(t,\tau) - R_{SM}(t,\tau) - R_{MS}(t,\tau), \tag{13}$$

where $R_{SS}(t,\tau)$ and $R_{MM}(t,\tau)$ are the IAFs of the all-pass mask $S(t)$ and the missing data mask $M(t)$, respectively, and $R_{SM}(t,\tau)$ and $R_{MS}(t,\tau)$ are two IAF cross-terms between $M(t)$ and $S(t)$. Using (4) and (8), the cross-term IAF $R_{SM}(t,\tau)$ is given by

$$\begin{aligned} R_{SM}(t,\tau) &= \sum_{i=1}^{N} s(t+\tau)\delta(t-t_i-\tau) \\ &= \sum_{b=1}^{B}\sum_{n=1}^{N_b} s(t+\tau)\delta(t-t_{bn}-\tau) \\ &= \sum_{b=1}^{B}\left[\sum_{n=1}^{N_b}\sum_{t_0=1}^{T}\delta(t-t_0,\tau-t_0+t_{bn})\right] \\ &= \sum_{b=1}^{B} R_{SM_b}(t,\tau), \end{aligned} \tag{14}$$

where $t_i \in \bar{\mathbb{S}}$ and $t_{bn} \in \bar{\mathbb{S}}_b$, and $R_{SM_b}(t,\tau) = \sum_{n=1}^{N_b}\sum_{t_0=1}^{T}\delta(t-t_0,\tau-t_0+t_{bn})$ is a rectangular strip with width N_b and is diagonally placed with a positive slope. Similarly, the cross-term IAF $R_{MS}(t,\tau)$ is given by

$$\begin{aligned} R_{MS}(t,\tau) &= \sum_{i=1}^{N} \delta(t-t_i+\tau)s(t-\tau) \\ &= \sum_{b=1}^{B}\sum_{n=1}^{N_b} \delta(t-t_{bn}+\tau)s(t-\tau) \\ &= \sum_{b=1}^{B}\left[\sum_{n=1}^{N_b}\sum_{t_0=1}^{T}\delta(t-t_0,\tau+t_0-t_{bn})\right] \\ &= \sum_{b=1}^{B} R_{MS_b}(t,\tau), \end{aligned} \tag{15}$$

where $R_{MS_b}(t,\tau) = \sum_{n=1}^{N_b}\sum_{t_0=1}^{T}\delta(t-t_0,\tau+t_0-t_{bn})$ is a rectangular strip with width N_b and is diagonally placed with a negative slope. Therefore, these two IAF cross-terms, $R_{SM}(t,\tau)$ and $R_{MS}(t,\tau)$, form B pairs of missing strips, each with width N_b. On the other hand, $R_{MM}(t,\tau)$ is expressed as

$$\begin{aligned} R_{MM}(t,\tau) &= \sum_{i=1}^{N}\delta(t-t_i+\tau)\sum_{k=1}^{N}\delta(t-t_k-\tau) \\ &= \sum_{b_1=1}^{B}\sum_{n_1=1}^{N_{b_1}}\delta(t-t_{b_1n_1}+\tau)\sum_{b_2=1}^{B}\sum_{n_2=1}^{N_{b_2}}\delta(t-t_{b_2n_2}-\tau) \\ &= \sum_{b_1=1}^{B}\sum_{b_2=1}^{B}\sum_{n_1=1}^{N_{b_1}}\sum_{n_2=1}^{N_{b_2}}\delta(t-t_{b_1n_1}+\tau)\delta(t-t_{b_2n_2}-\tau) \\ &= \sum_{b_1=1}^{B}\sum_{b_2=1}^{B}\sum_{n_1=1}^{N_{b_1}}\sum_{n_2=1}^{N_{b_2}}\delta\left(t-\frac{t_{b_1n_1}+t_{b_2n_2}}{2},\tau\pm\frac{t_{b_1n_1}-t_{b_2n_2}}{2}\right). \end{aligned} \tag{16}$$

Note that the entries of the Delta function in the last line take non-zero values only when $t_{b_1n_1} - t_{b_2n_2}$ is zero or an even integer. These entries defined in the above expression (16) can be classified into two groups. Entries in the first group belong to the same bursts and are clustered around the time axis (i.e., $\tau = 0$ axis), whereas those in the second group correspond to different bursts and are clustered away from the time axis. These two groups of entries are respectively expressed as

$$
\begin{aligned}
R_{MM}(t,\tau) &= R_{MM}^{\text{auto}}(t,\tau) + R_{MM}^{\text{cross}}(t,\tau) \\
&= \sum_{b=1}^{B}\sum_{n_1=1}^{N_b}\sum_{n_2=1}^{N_b} \delta\left(t - \frac{t_{bn_1}+t_{bn_2}}{2}, \tau \pm \frac{t_{bn_1}-t_{bn_2}}{2}\right) \\
&\quad + \sum_{b_1=1}^{B}\sum_{\substack{b_2=1 \\ b_2\neq b_1}}^{B}\sum_{n_1=1}^{N_{b_1}}\sum_{n_2=1}^{N_{b_2}} \delta\left(t - \frac{t_{b_1n_1}+t_{b_2n_2}}{2}, \tau \pm \frac{t_{b_1n_1}-t_{b_2n_2}}{2}\right).
\end{aligned} \tag{17}
$$

For illustration purposes, examples of missing mask entries are depicted in Fig. 2(d) where the auto-burst terms are depicted in red, whereas the cross-burst terms are depicted in yellow.

As a result of the above discussions, the overall difference in the mask IAF due to the missing data samples can be defined as

$$
\begin{aligned}
R_D(t,\tau) &= R_{SS}(t,\tau) - R_{RR}(t,\tau), \\
&= R_{SM}(t,\tau) + R_{MS}(t,\tau) - R_{MM}(t,\tau).
\end{aligned} \tag{18}
$$

The missing entries of IAF, located at positions of unit-valued entries of $R_D(t,\tau)$, induce a high level of undesired artifacts in the WVD of the received signal. Each missing IAF strip causes a convoluting sinc function applied to the original WVD. As a result, the missing samples yield sinc-like artifacts in the WVD. Therefore, due to the superimposition of different sinc-like patterns created by the combination of different bursts of missing data, these artifacts are manifested as a highly aliased structure near the true signal IF signatures in the WVD, thereby greatly obscuring the proper identification of the true TF signatures. In the underlying burst missing data case, the clear patterns of the artifacts, with the energy highly localized around the true IFs, greatly differ to the results caused by random missing samples, as reported in [18], where the artifacts are uniformly distributed over the frequency. The burst missing samples in the IAF also cause sinc-like artifacts in the ambiguity domain. As we discussed earlier, this fact makes the suppression of artifacts due to missing samples more difficult through simple ambiguity-domain filtering. Also note that, unlike additive noise, the effects of these artifacts cannot be mitigated by increasing the signal power.

In practice, the length of the rectangular window along the lag (τ) dimension varies as a function of t as follows,

$$
Q(t) = T - |T + 1 - 2t|, \quad t = 1, ...T. \tag{19}
$$

Due to zero-padding created by this window effect, the total number of non-zero entries of $R_{ss}(t,\tau)$ is reduced to $Q(t)$ at a given time t. Thus, for $s(t)$ with T samples, the total number of non-zero entries of $R_{ss}(t,\tau)$ will be equal to $T^2/2$ if T is even, and $(T^2+1)/2$ if T is odd. Similar to the uniform missing data case [18], for an even value of T, the number of unit-value entries of $R_D(t,\tau)$ in the presence of

N missing data samples will be equal to the number of missing entries in $R_{rr}(t,\tau)$, which can be well approximated as

$$\tilde{N} = NT - N^2/2. \tag{20}$$

B. Demonstration Examples

To visualize the above discussions regarding the effects of burst missing samples, we consider a single-component FM signal, for which the instantaneous phase law is given by,

$$\phi(t) = 0.05t + 0.05t^2/T + 0.1t^3/T^2, \tag{21}$$

where $t = 1, ..., T$, with T being selected as 128. In order to clearly demonstrate the effect of burst missing samples on the IAF, the TFR, and the AF, we only consider the noise-free case.

Fig. 1(a) shows the real-part of the original signal waveform without missing samples. Fig. 1(b) shows the IAF magnitude of the original signal. In Fig. 1(b), due to the windowing effect created by zero-padding of the time-domain data, the non-zero entries of the IAF are shown in the diamond shaped region, as depicted in (19). The magnitude of the IAF is constant within the diamond-shaped region, because the underlaying FM signal has only one component. Fig. 1(c) shows the corresponding WVD. In this figure, the WVD is able to obtain a clear TFR, except for some cross-term distortions in the center region due to the bilinear nature of the WVD corresponding to the underlying non-linear FM signal. Fig. 1(d) shows the AF whose magnitude is symmetric about the origin.

In the following, we present several examples to demonstrate the effects of burst missing samples. In all these examples, the total number of missing samples is 48, which amounts to 37.5% of the data length. We first consider 6 missing bursts with an equal width of 8 samples. We then consider two different cases, which respectively have 3 missing bursts with a burst width of 16 samples, and 12 missing bursts with 4 samples in each burst, to examine the effect of the burst width. Finally, we consider an example of 6 missing bursts with mixed burst widths.

1) Missing Bursts with Equal Widths: In the first example, we consider missing data bursts with an equal number of missing samples in each burst. The missing samples form 6 bursts in total, with 8 samples in each burst.

Fig. 2(a) shows the real part of the received signal with 48 burst missing data samples, where missing data positions are marked with red dots. Fig. 2(b) shows the corresponding IAF magnitude. The missing entries of the IAF are related to the burst missing samples, and appear grouped as well, as each missing sample in the time-domain waveform causes two diagonal missing lines in the IAF. From (20), the total number of missing IAF entries in the diamond shaped region is 4992, which amounts to about 61% of

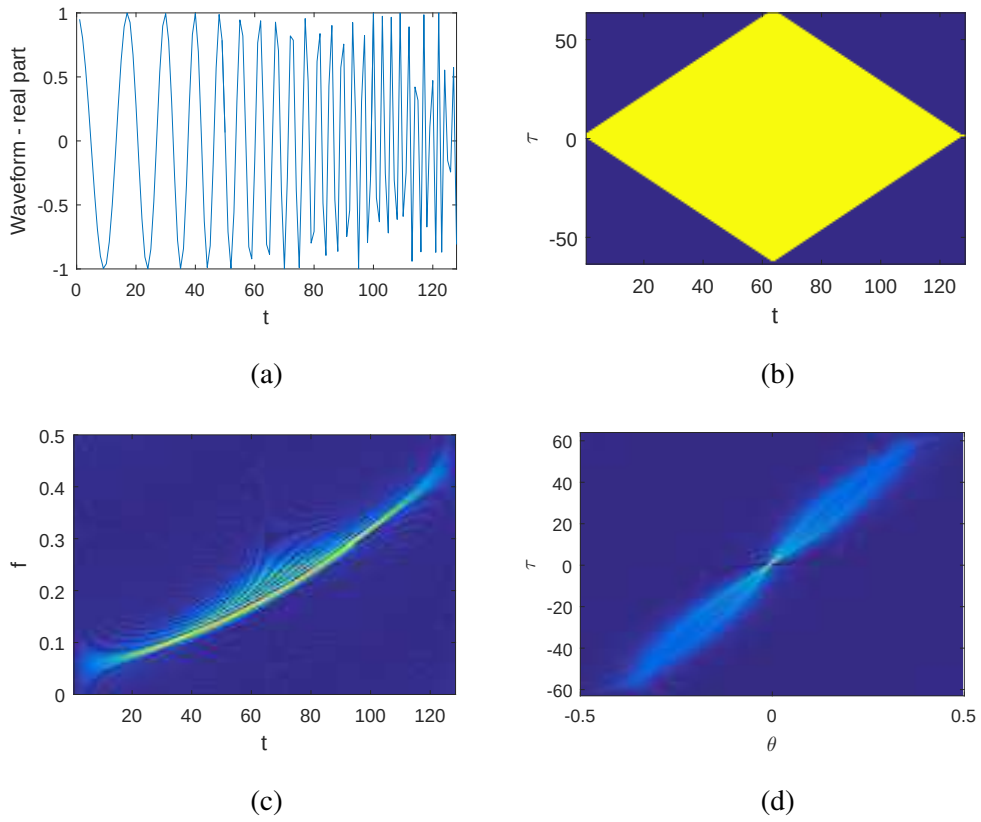

Fig. 1 The original signal: (a) Real part of the signal; (b) The IAF; (c) The WVD; (d) The AF.

the total entries of the original IAF. Fig. 2(c) shows missing IAF entries of the aforementioned received signal, marked in yellow color. These unit-valued entries denote $R_D(t,\tau)$, as defined in (18). Fig. 2(d) illustrates different mathematical terms related to these missing entries, defined in (14)–(16). The green and blue rectangle strips respectively show the components of $R_{SM}(t,\tau)$ and $R_{MS}(t,\tau)$, whereas the red and yellow diamond shaped regions respectively correspond to the auto-burst and cross-burst intersections.

Fig. 2(e) shows the corresponding WVD. The aliasing structure created as a result of superimposed sinc-like artifacts patterns, induced due to different groups of burst missing data, is clearly visible in Fig. 2(e). Because each missing data burst has the same width, the artifacts are linked with a single sinc function. Fig. 2(f) shows the AF which, when compared to Fig. 1(d), is clearly blurred around the auto-terms. Note that, unlike the random missing sample case, where strong artifacts exist along the $\tau = 0$ axis, such artifacts are spread around auto-terms in Fig. 2(f) with a convolutive sinc function, making the auto-term identification and artifact mitigation difficult.

2) Effects of the Burst Width on the TFR: In this example, we demonstrate the effects of the burst width, N_b, on the corresponding TFRs. The same signal as defined in (21) is assumed, and missing bursts

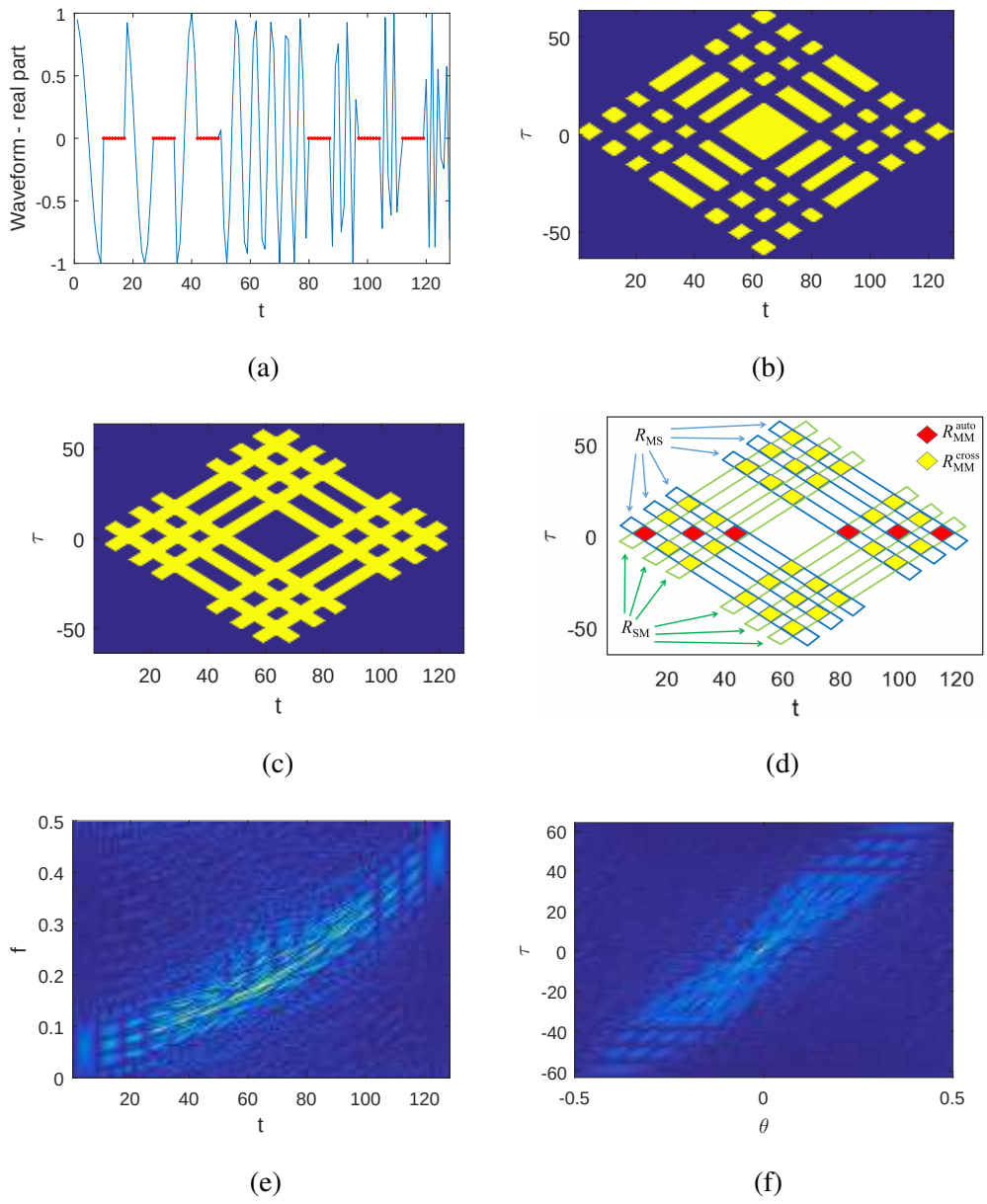

Fig. 2 The received signal with 48 (i.e. 37.5%) missing samples, with 6 bursts of missing samples, each burst having width of 8 samples: (a) Real part of the signal; (b) The IAF; (c) Missing entries of the IAF; (d) Explanation of different terms regarding missing IAF entries; (e) The WVD; (f) The AF.

with an equal width are considered. To clearly examine the effects of the burst width, the total number of missing samples, N, is kept the same. We consider two cases, respectively, with the burst widths equal to 16 and 4, and compare the findings with the results obtained in the previous example, where the missing bursts with an equal width of 8 samples are considered.

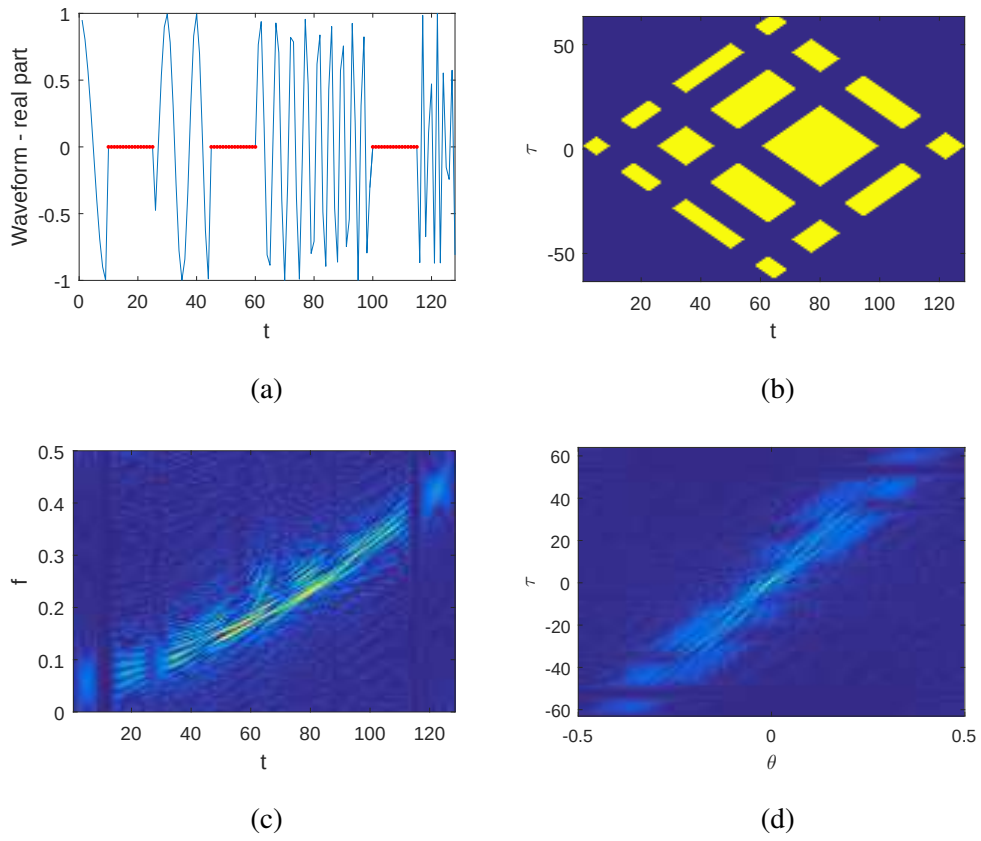

Fig. 3 The received signal with 48 missing samples, with 3 bursts of missing samples, each burst having width of 16 samples: (a) Real part of the signal; (b) The IAF; (c) The WVD; (d) The AF.

Fig. 3(a) shows the real part of the received signal with 48 burst missing data samples, where the missing samples form a total of 3 bursts, with 16 samples in each burst. Fig. 3(b) shows the IAF with clear burst missing entries. Figs. 3(c) and 3(d), respectively, show the WVD and the AF where aliasing structures due to sinc-like artifact patterns are clearly visible in both plots. In Fig. 3(c), the artifacts with as high energy peaks as the true signal components are closely concentrated around the true IFs, making the identification of the true signal components challenging. Because of the wide missing sample burst width, the sinc function has a narrower spreading. The artifacts in the AF are clearly visible and are highly concentrated near the auto-terms with comparable amplitudes. We will see in the subsequent section that this poses a great challenge for TF kernels in terms of cross-term suppression and auto-term preservation, resulting in poor TFR results.

Fig. 4(a) shows the real part of the received signal with 48 burst missing data samples, where the total number of bursts is 12, with each burst containing 4 missing samples. Figs. 4(b) and 4(c), respectively, show the corresponding IAF and the WVD. As seen in Fig. 4(c), the aliasing structure is created as

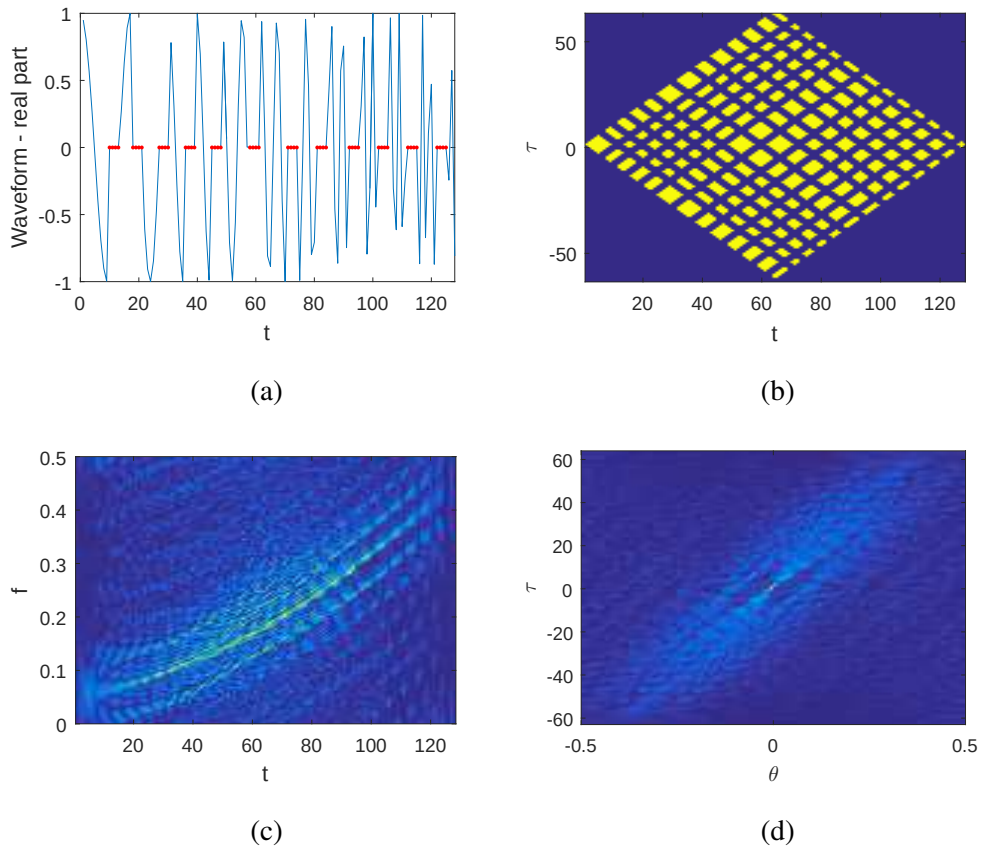

Fig. 4 The received signal with 48 missing samples, with 12 bursts of missing samples, each burst having width of 4 samples: (a) Real part of the signal; (b) The IAF; (c) The WVD; (d) The AF.

a result of superimposed sinc-like artifact patterns, which are spread with a greater separation in the frequency domain because of the narrower missing data bursts. In this case, the multiple resolved aliasing components are clearly observed. Similar observations can be made for the AF as shown in Fig. 4(d).

These examples confirm that, for the same number of burst missing samples, the given FM signal can be better reconstructed for the higher number of missing data bursts with a small number of missing samples in each burst, compared to the case that involves a smaller number of groups of the burst missing data with larger widths. The bursts of missing data with larger widths also adversely affect the shape of the reconstructed signal, along with quality.

3) Missing Bursts with Varying Widths: In this example, we consider missing data bursts with different number of missing samples in each burst, i.e., the width N_b varies for different bursts. For comparison purposes, we consider the same signal as defined in (21), and the total number of missing samples remains 48. The 6 missing bursts respectively contain 11, 9, 4, 6, 8 and 10 missing samples.

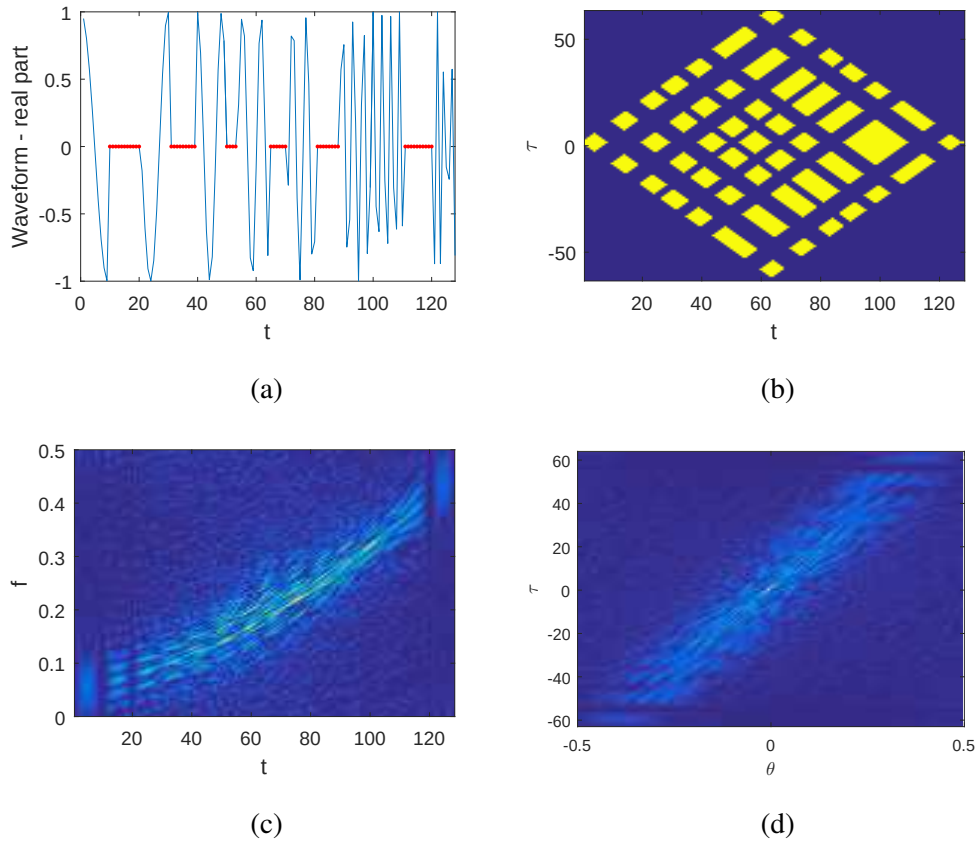

Fig. 5 The received signal with 48 missing samples, with 6 bursts of missing samples, each burst having different number of missing samples: (a) Real part of the signal; (b) The IAF; (c) The WVD; (d) The AF.

Figs. 5(a)–5(d), respectively, show the real part of the received signal, the corresponding IAF, the WVD, and the AF. As seen in Fig. 5(c), the WVD of the received signal is comparable to the WVD of the Fig. 2(e). However, the varying widths of the missing data bursts make the artifacts more random. In this case, the AF shown in Fig. 5(d) also becomes blurred with an unclear structure.

IV. Sparse Reconstruction Using MI-SR

In this section, we describe the proposed MI-SR approach for sparse TFR recovery. At each time instant t, we denote $\mathbf{x}^{(t)}$ as the $P \times 1$ TF vector, and $\mathbf{y}^{(t)}$ as the $Q(t) \times 1$ IAF vector, where $Q(t)$ is defined in (19). These two vectors are related by the following formula,

$$\mathbf{y}^{(t)} = \mathbf{D}(t)\mathbf{x}^{(t)}, \quad \forall t, \tag{22}$$

where $\mathbf{D}(t)$ is the $Q(t) \times P$ dictionary matrix performing 1-D IDFT. Note that $\mathbf{D}(t)$ is time-dependent because of the different zero-padding patterns at different time locations. The objective of the MI-SR is

to provide a robust reconstruction of TFR vector $\mathbf{x}^{(t)}$ from $\mathbf{y}^{(t)}$, where $\mathbf{y}^{(t)}$ is subject to missing entries as discussed in the precious section. The MI-SR works well for both random as well as burst missing data sample scenarios. Note that the TFR matrix is obtained by horizontally concatenating the vector $\mathbf{x}^{(t)}$ over all time instants $t = 1, 2, ..., T$ as $\mathbf{X} = [\mathbf{x}^{(1)}, \mathbf{x}^{(2)}, ..., \mathbf{x}^{(T)}]$.

As all the operations in this section are performed at each time instant t, we omit superscript (t) from the expressions of $\mathbf{x}^{(t)}$ and $\mathbf{y}^{(t)}$ for notational simplicity. Similarly, we also simplify $\mathbf{D}(t)$ as $\mathbf{D}$, and $Q(t)$ as Q.

A. Problem Formulation

The MI-SR is applied in the IAF domain because the IAF of FM signals is stationary. Denote P as the number of grid points in the frequency domain with $f_p,\ p = 1, ..., P$, being the corresponding frequencies. Consider a K-sparse vector $\mathbf{x}^{(t)}$ with $K \ll P$, where the sparsity K is assumed to be known or can be estimated. On the other hand, the vector $\mathbf{y}$ consists of two components. The first component is vector $\mathbf{y}_r = [y_{r_1}, y_{r_2}, ..., y_{r_{Q_r}}]^T$ which contains Q_r measured IAF elements which do not change during the MI-SR operation, whereas the second component is vector $\mathbf{y}_m = [y_{m_1}, y_{m_2}, ..., y_{m_{Q_m}}]^T$ which contains $Q_m = Q - Q_r$ missing IAF entries and will be iteratively updated. These two components are, respectively, represented as

$$\mathbf{y}_r = \mathbf{\Gamma}_r \mathbf{y}, \quad \mathbf{y}_m = \mathbf{\Gamma}_m \mathbf{y}, \tag{23}$$

where $\mathbf{\Gamma}_r$ is a $Q_r \times Q$ masking matrix that extracts the measured elements from vector $\mathbf{y}$, whereas $\mathbf{\Gamma}_m$ is a $Q_m \times Q$ masking matrix that extracts the missing elements.

Similarly, we can separate the dictionary matrix $\mathbf{D}$ into two parts, where the $Q_r \times P$ matrix $\mathbf{D}_r = \mathbf{\Gamma}_r \mathbf{D}$ extracts the rows of $\mathbf{D}$ corresponding to the measured IAF entries in $\mathbf{y}_r$, and the $Q_m \times P$ matrix $\mathbf{D}_m = \mathbf{\Gamma}_m \mathbf{D}$ contains the rows of $\mathbf{D}$ corresponding to the missing IAF entries in $\mathbf{y}_m$.

Based on the measured data entries while excluding the burst missing samples, (22) becomes,

$$\mathbf{y}_r = \mathbf{D}_r \mathbf{x}. \tag{24}$$

Considering the sparse nature of the signal in the TF domain, the non-zero entries of $\mathbf{x}$ can be estimated using sparse signal recovery techniques, as a solution to the following ℓ_0-norm minimization problem:

$$\hat{\mathbf{x}} = \arg\min_{\mathbf{x}} ||\mathbf{x}||_0 \quad \text{subject to} \quad \mathbf{D}_r \mathbf{x} = \mathbf{y}_r. \tag{25}$$

The above problem can be solved using greedy algorithms such as the OMP. With burst missing samples, however, the direct application of sparse reconstruction in the above expression does not yield robust TFRs. In the following, we propose a new technique that iteratively reconstruct the TFR and then estimate the missing IAF entries.

B. Proposed MI-SR Algorithm

The concept of exploiting iterative frequency spectrum estimation and missing sample filling is inspired by the MIAA [41] which was developed for the spectrum estimation of stationary signals. In each iteration, sequential estimation of the Capon spectrum is performed to minimize the weighted least squares between the received signal vector and its estimates. Then, missing samples are recovered based on the estimated frequencies and their coefficients. The Capon spectrum estimation and missing sample recovery are iterated for performance improvement. While the MIAA cannot be directly applied to FM signals which are non-stationary, we can take advantage of the stationary Fourier transform relationship between the IAF and the TFR and thus apply the MIAA in TFR reconstruction using these two domains [40]. In this paper, we use OMP, in lieu of the Capon method, for the spectrum estimation in each iteration. Because of the clear sparsity of the TFR structures, the proposed method yields more effective TFR reconstruction and better performance. For each time instant t, the entire process of the proposed MI-SR algorithm is summarized below:

(i) The outer iteration counter, j, is set to 1. Based on the available IAF entries at time t, the input vector and the corresponding dictionary matrix are, respectively, initialized as $\mathbf{y}_r^{(0)} = \mathbf{y}_r$ and $\mathbf{D}_r^{(0)} = \mathbf{D}_r$. Similarly, the missing data vector and the corresponding dictionary matrix are initialized as $\mathbf{y}_m^{(0)} = \mathbf{y}_m$ and $\mathbf{D}_m^{(0)} = \mathbf{D}_m$, respectively. The signal sparsity K is assumed to be known or can be estimated.

(ii) The *residual vector* and the index set are, respectively, initialized as $\mathbf{e}_0 = \mathbf{y}^{(j-1)}$ and $\Phi_0 = \emptyset$. The inner (OMP) iteration counter i within each outer iteration is set to 1.

(iii) The index ϕ_i is deterministically obtained as a solution to the following optimization problem:

$$\phi_i = \arg \max_{p \in \{1,\ldots,P\}} \left| \mathbf{e}_{i-1}^H \mathbf{d}_p^{(j-1)} \right|, \tag{26}$$

where $\mathbf{d}_p^{(j-1)}$ is the pth column of the dictionary $\mathbf{D}^{(j-1)}$.

(iv) The index set is updated as

$$\Phi_i = \Phi_{i-1} \cup \{\phi_i\}, \tag{27}$$

and the dictionary matrix of the selected columns is updated as

$$\bar{\mathbf{D}}^{(j;i)} = [\bar{\mathbf{D}}^{(j;i-1)} \;\; \mathbf{d}_{\phi_i}^{(j-1)}]. \tag{28}$$

Note that the total number of columns in the full column-rank dictionary matrix $\bar{\mathbf{D}}^{(j;i)}$ is i, with $\bar{\mathbf{D}}^{(j;0)}$ indicating an empty matrix.

(v) At each inner iteration, a new signal estimate is uniquely obtained from the following formula based on the available dictionary matrix:

$$\hat{\mathbf{x}}_i = \arg\min_{\mathbf{x}_i} ||\mathbf{y}^{(j-1)} - \bar{\mathbf{D}}^{(j;i)}\mathbf{x}_i||_2. \tag{29}$$

(vi) The new estimate of the IAF vector, $\mathbf{v}_i$, and the residual vector, $\mathbf{e}_i$, are obtained at each round as

$$\begin{aligned} \mathbf{v}_i &= \bar{\mathbf{D}}^{(j;i)}\hat{\mathbf{x}}_i, \\ \mathbf{e}_i &= \mathbf{y}^{(j-1)} - \mathbf{v}_i. \end{aligned} \tag{30}$$

Note that the residual $\mathbf{e}_i$ is always orthogonal to the columns of $\bar{\mathbf{D}}^{(j;i)}$. Ideally, in order to recover the entire signal with probability one, the residual $\mathbf{e}_k$ after the Kth inner iteration should be zero.

(vii) The inner iteration counter i is incremented by 1, and steps (iii)–(vi) are repeated until $i = K$.

(viii) At the end of the jth outer iteration, the value of the ϕ_ith non-zero component of the estimated signal $\hat{\mathbf{x}}^{(j)}$ is given by the ith component of $\hat{\mathbf{x}}_i$. Using the relationship shown in (22), the new estimate of the IAF vector $\hat{\mathbf{y}}^{(j)}$ is obtained as

$$\hat{\mathbf{y}}^{(j)} = \mathbf{D}\hat{\mathbf{x}}^{(j)}. \tag{31}$$

Note that only the missing entries of the original IAF vector, $\mathbf{y}_m^{(0)}$, are updated with the corresponding entries of the above new estimated IAF vector, i.e.,

$$\mathbf{y}_m^{(j)} = \mathbf{\Gamma}_m\hat{\mathbf{y}}^{(j)}. \tag{32}$$

(ix) The outer iteration counter, j, is incremented by 1 and steps (ii)–(viii) are repeated until the squared error between two subsequent signal estimates falls below a predefined threshold value, ϵ, i.e.,

$$||\hat{\mathbf{x}}^{(j)} - \hat{\mathbf{x}}^{(j-1)}||_2^2 < \epsilon. \tag{33}$$

C. Applying MI-SR to Kerneled IAF

Note that cross-terms are a byproduct of bilinear operation in the quadratic TFR which exist even when there are no missing samples. Therefore, while the proposed MI-SR is effective in mitigating the effects of missing samples, it cannot suppress the effects of cross-terms. However, we can combine the TF kernel operation and the proposed MI-SR algorithm. In so doing, the combination of TF kernel and MI-SR yields superior performance in IF signature estimation as it mitigates both effects of missing samples and cross-terms.

Once we apply the TF kernels as described in Section II-C by taking the AOK as an example, we transform the kerneled AF to kerneled IAF by performing the 1-D Fourier transform with respect to

frequency shift θ. In this case, each column of the obtained IAF matrix is the IAF vector $\mathbf{y}^{(t)}$ corresponding to time instant t, and the procedures described in Section IV-B can be applied.

It is noted that, after applying the kernel, the IAF matrix generally no longer contains missing entries because the kernel effectively performs convolution with respect to t and thus fills the missing positions based on the unkerneled IAF values of the neighboring time instants. However, as we can see in the simulation results in the next section, the values in these originally missing entries filled by the AOK alone are not accurate and still suffer from the effect of missing samples. Updating using the proposed MI-SR can mitigate the effects due to missing samples. In this case, the MI-SR is used only to update the IAF entries at positions that are missed in the unkerneled IAF.

D. Computational Complexity

For a *K*-sparse signal in $\mathbb{R}^d$ with $K \ll d$, the computational complexity of the MI-SR is given by $\mathcal{O}(I_{\text{MI}-\text{SR}} K^2 d \ln d)$, with $I_{\text{MI}-\text{SR}}$ being the number of iterations. The computational cost of the AOK for each time instant is in order of $\mathcal{O}(I_{\text{AOK}} C^2)$, where I_{AOK} is the required number of iterations to solve the optimization problem given in (11) and C denotes the number of angle and radius samples in the polar-coordinate STAF. Typically, $C = 2T$ is considered, and in case of the MI-SR, $d = T$ is used. Using this information, the computational complexity of the MI-SR and the AOK respectively becomes $\mathcal{O}(I_{\text{MI}-\text{SR}} K^2 T \ln T)$ and $\mathcal{O}(I_{\text{AOK}} 4T^2)$. The computational cost of the MIAA is given by $\mathcal{O}(I_{\text{MIAA}}[2P(N_g)^2 + (N_g)^3])$ [52], where, for the time-domain MIAA, $N_g = T - N$ is the total number of observed data samples. When the MIAA is applied to the IAF, N_g becomes the total number of available IAF entries described in (19) and (20). Because the value of N_g obtained in the IAF domain is much higher than that obtained in the time domain, the computational complexity of the IAF-domain MIAA is high. The MIAA typically requires $I_{\text{MIAA}} = 10$ to 15 iterations to converge [53], whereas $I_{\text{MI}-\text{SR}}$ and I_{AOK} typically assume small values. With this information, we can confirm that the computational complexity of the MI-SR is considerably lower than that of the AOK and the time-domain MIAA, whereas its computational advantage to the IAF-domain MIAA is even more pronounced.

V. Simulation results

In this section, we present the performance of the proposed MI-SR algorithm applied to both unkerneled and kerneled IAFs. These methods are compared with two existing approaches, namely, the signal-dependent AOK approach [18] and the MIAA based on data interpolation [40]. For reference, we also show the TFR results obtained by applying the MIAA to the time-domain data. To emphatically demonstrate the effectiveness of the proposed MI-SR in the presence of burst missing samples, TFR

results obtained using these approaches are compared in Section V-A. Further, quantitative evaluation and comparison in terms of their root mean square errors (RMSE) and energy concentration measures are respectively provided in Sections V-B and V-C. In Section V-D, we analyze the effects of the percentage of the burst missing samples on the TFR reconstruction performance. TFR reconstruction in the case of a multi-component non-linear FM signal is considered in Section V-E. In addition, the required execution time is compared in Section V-F as the measure of the computational complexity of these approaches.

A. Comparison of Reconstructed TFRs

Figs. 6–9 provide qualitative comparison of the TFRs obtained using different approaches in the presence of 48 missing data samples, and these results respectively correspond to the received signal depicted in Figs. 2–5 with different burst missing patterns. In each figure, the sub-figures (a) through (e) respectively show TFRs obtained by applying the MIAA to the time domain signal, by applying the MIAA in the IAF domain, using the AOK, the MI-SR and, finally, by applying the MI-SR to the kerneled IAF.

Fig. 6 shows the TFRs obtained using the 5 different approaches, as mentioned above, for the received signal from Fig. 2(a) with 48 missing samples grouped in 6 bursts, each having a width of 8 samples. As seen in Fig. 6(a), the MIAA approach, when applied to the time domain data with burst missing samples, fails completely to obtain a clear TFR of the non-stationary FM signal because the MIAA is designed to handle stationary signals. The artifacts are scattered around the true IFs in the TF domain, obscuring identification of the true IFs. With the MIAA applied in the IAF domain, the TFR in Fig. 6(b) shows significant improvement, benefitting from the stationarity of the IAF with respect to lag, τ, at each time instant. However, cross-terms are observed in the center region due to the bilinear distribution nature. In Fig. 6(c), when the AOK is applied, excessive thickening of the TFR is observed in the center region and aliasing at both sides remains an issue. As seen from Fig. 6(d), the proposed MI-SR overcomes these shortcomings and produces superior TFR, except a small number of TF points with insignificant biases. As shown in Fig. 6(e), the results are further refined by applying the AOK method before performing the MI-SR technique.

Fig. 7 compares the TFRs obtained from the same five different approaches for the signal depicted in Fig. 3(a) where the 48 missing samples are clustered into 3 bursts, and each burst contains a high number of 16 missing samples. As explained in the previous section, in this case, the relatively large widths of the missing bursts pose challenges in the TFR reconstruction. In Fig. 7(a), the aliasing components around the true IFs are less structured, making it even more difficult to recognize the true signal signatures. In Fig. 7(b), and unlike Fig. 6(b) where the cross-terms are predominant in the center region, the cross-terms are

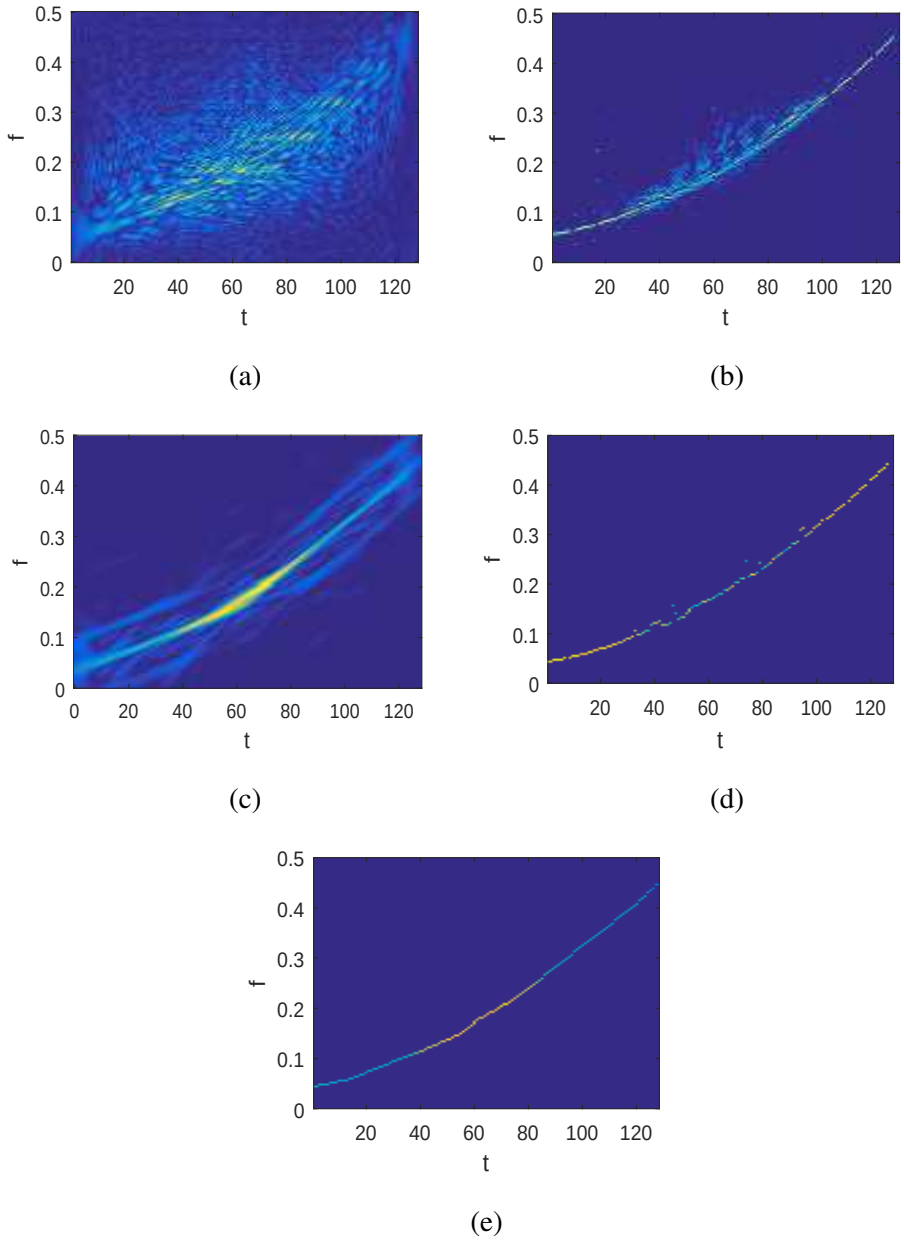

Fig. 6 Scenario 1: Comparison of TFRs obtained using 5 different approaches, applied to the received signal depicted in Fig. 2(a), where the 48 missing samples are clustered into 6 bursts, each containing 8 missing samples. (a) MIAA applied to the time domain data; (b) MIAA applied to the IAF; (c) AOK; (d) MI-SR; (e) MI-SR applied to the kerneled IAF.

more severely scattered, causing blurring of the true signal signatures. Excessive broadening and blurring is observed in the TFR of Fig. 7(c), obtained using the AOK. In Fig. 7(d), the MI-SR gives improved reconstruction results. It is clear from Figs. 7(b) and 7(d) that the signal IF signatures reconstructed from

both the MIAA and the MI-SR are less perfect because of the insufficient number of IAF entries owing to the long missing bursts. When applying the MI-SR to the kerneled IAF, as shown in Fig. 7(e), we successfully recovers the TFR with a consistent IF signature, although there is a minor IF bias in the beginning at around $t = 25$.

Fig. 8 shows the TFR reconstruction results for the signal depicted in Fig. 4(a), in which the 48 missing samples are clustered into 12 bursts with 4 missing samples in each burst. When comparing Fig. 8(a) with Fig. 4(c), the direct application of the MIAA to the time-domain data slightly reduces the aliasing but the TFR is more distorted for the portion with $t > 60$. Fig. 8(b) shows the TFR obtained by applying the MIAA in the IAF domain, in which excessive interfering cross-terms are observed in the center region. Fig. 8(c) shows that the AOK produces consistent TFR for all the time instants, while the frequency resolution is limited and there are aliasing components located in both sides of the true IF signature. Fig. 8(d) shows that, with the use of the proposed MI-SR, a distinct TFR signature is achieved and the undesired effects of the artifacts observed in Figs. 8(a)–8(c) are mitigated as a result of interpolation of the missing IAF entries. The proposed MI-SR recovered the IF signature except a few sporadic points scattered in the cross-term region. In Fig. 8(e), the combination of the AOK and the proposed MI-SR yields perfect cross-term mitigation and IF signature recovery. Compared to Figs. 6 and 7, it can be observed that the case presented in Fig. 8 with short missing data bursts results in more consistent TFR reconstruction with less distortions.

In Fig. 9, we present the TFRs produced using the aforementioned approaches for the signal depicted in Fig. 5(a), where the 48 missing samples are grouped into 6 bursts with a varying number of missing samples in each burst, ranging from 4 to 11. Overall, the results are closely comparable to those depicted in Fig. 6 for the case that the missing samples are clustered into 6 bursts but with the same cluster width. In Fig. 9(a), obtained from the direct application of the MIAA to the time-domain data, the aliasing is less structured, whereas slightly lower cross-terms are observed in Fig. 9(b) when the MIAA is applied to the IAF. The result obtained from the AOK, depicted in Fig. 9(c), shows a similar pattern where the true IF is relatively concentrated and is flanked by artifacts on both sides. As shown in Fig. 9(d), the proposed MI-SR provides consistent IF estimation performance except for several TF points with insignificant biases. When the MI-SR is applied to the kerneled IAF, as shown in Fig. 9(e), the resulting IF estimates are consistent without interruptions.

All these examples, which contain sufficient variety in terms of the number of missing data bursts and their widths, confirm the superiority of the proposed MI-SR technique over the MIAA and the AOK, in terms of the TFR reconstruction results. We also demonstrate that the few cross-term points observed in the TFRs obtained using the MI-SR alone, which are inevitable due to bilinear nature of the TFRs,

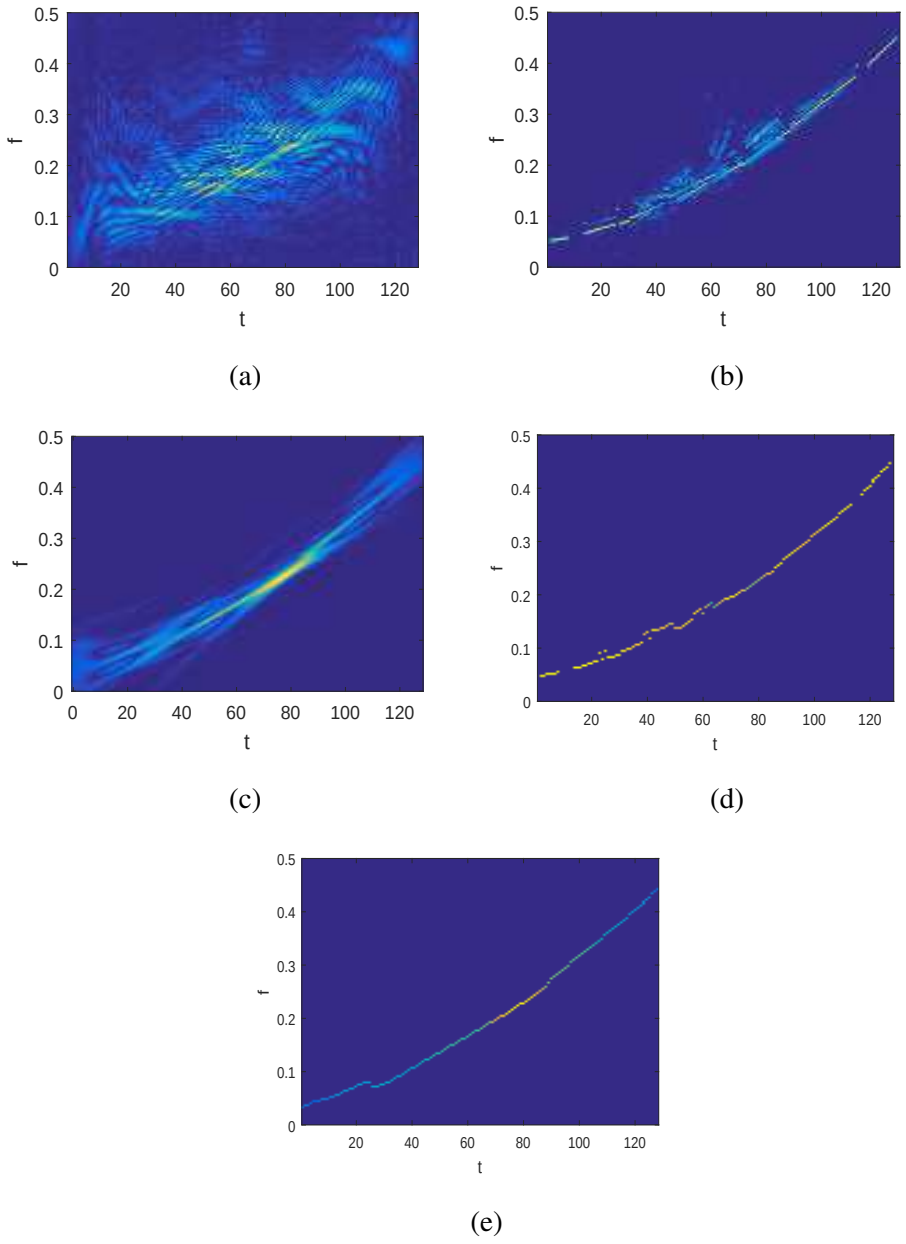

Fig. 7 Scenario 2: Comparison of TFRs obtained using 5 different approaches, applied to the received signal depicted in Fig. 3(a), where the 48 missing samples are clustered into 3 bursts, each containing 16 missing samples. (a) MIAA applied to the time domain data; (b) MIAA applied to the IAF; (c) AOK; (d) MI-SR; (e) MI-SR applied to the kerneled IAF.

can be mitigated by combining with the data-dependent kernel operation in order to achieve robust TFRs with a high fidelity.

It is noted that, while we used OMP in this paper to perform iterative TFR reconstruction, other CS

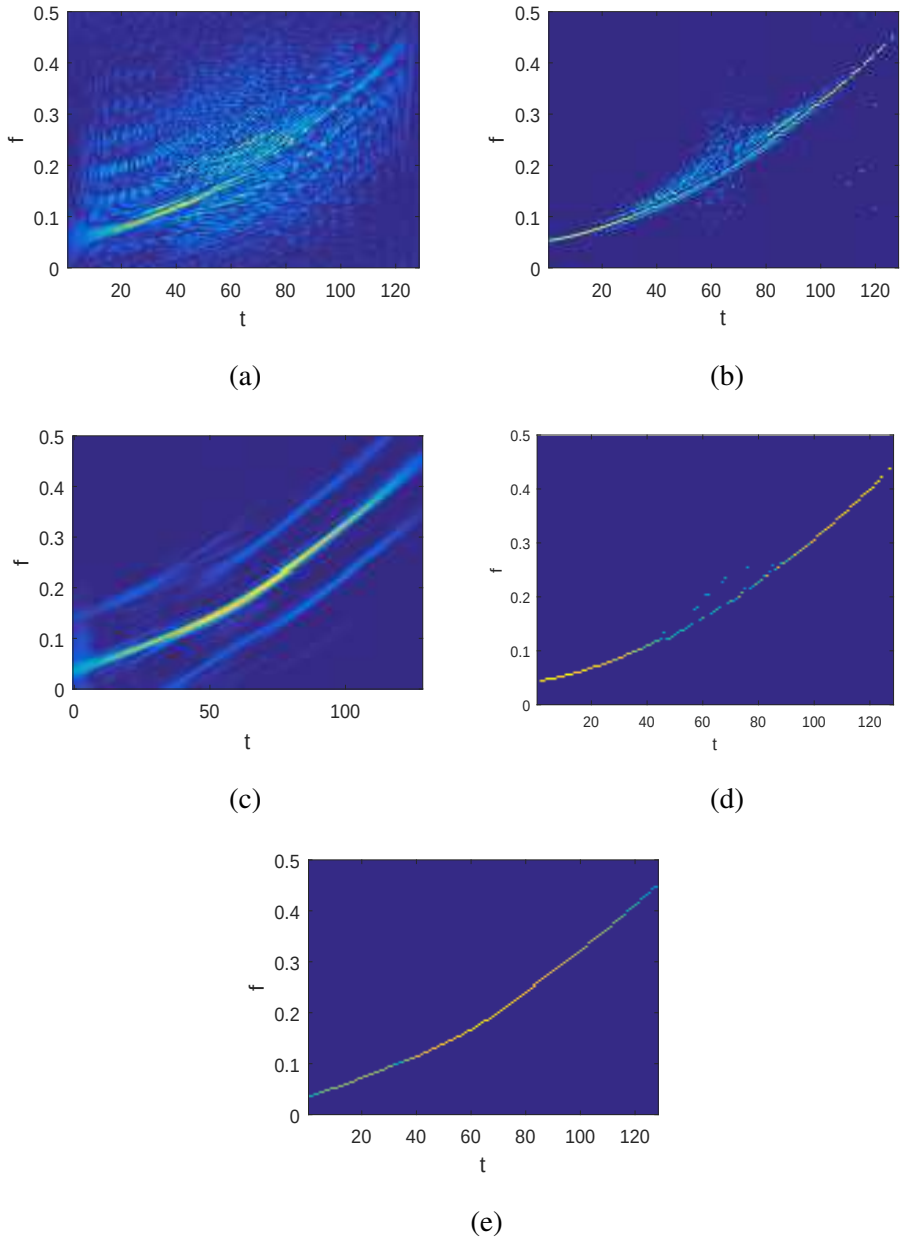

Fig. 8 Scenario 3: Comparison of TFRs obtained using different approaches, applied to the received signal depicted in Fig. 4(a), where the 48 missing samples are clustered into 12 bursts, each containing 4 missing samples. (a) MIAA applied to the time domain data; (b) MIAA applied to the IAF; (c) AOK; (d) MI-SR; (e) MI-SR applied to the kerneled IAF.

methods can also be used. In particular, the Bayesian compressive sensing [44]–[47] can be modified to account for the continuous-IF structure [19], [39]. Therefore, using such techniques, in lieu of the OMP in the proposed MI-SR, may yield improved performance but generally at a higher computational

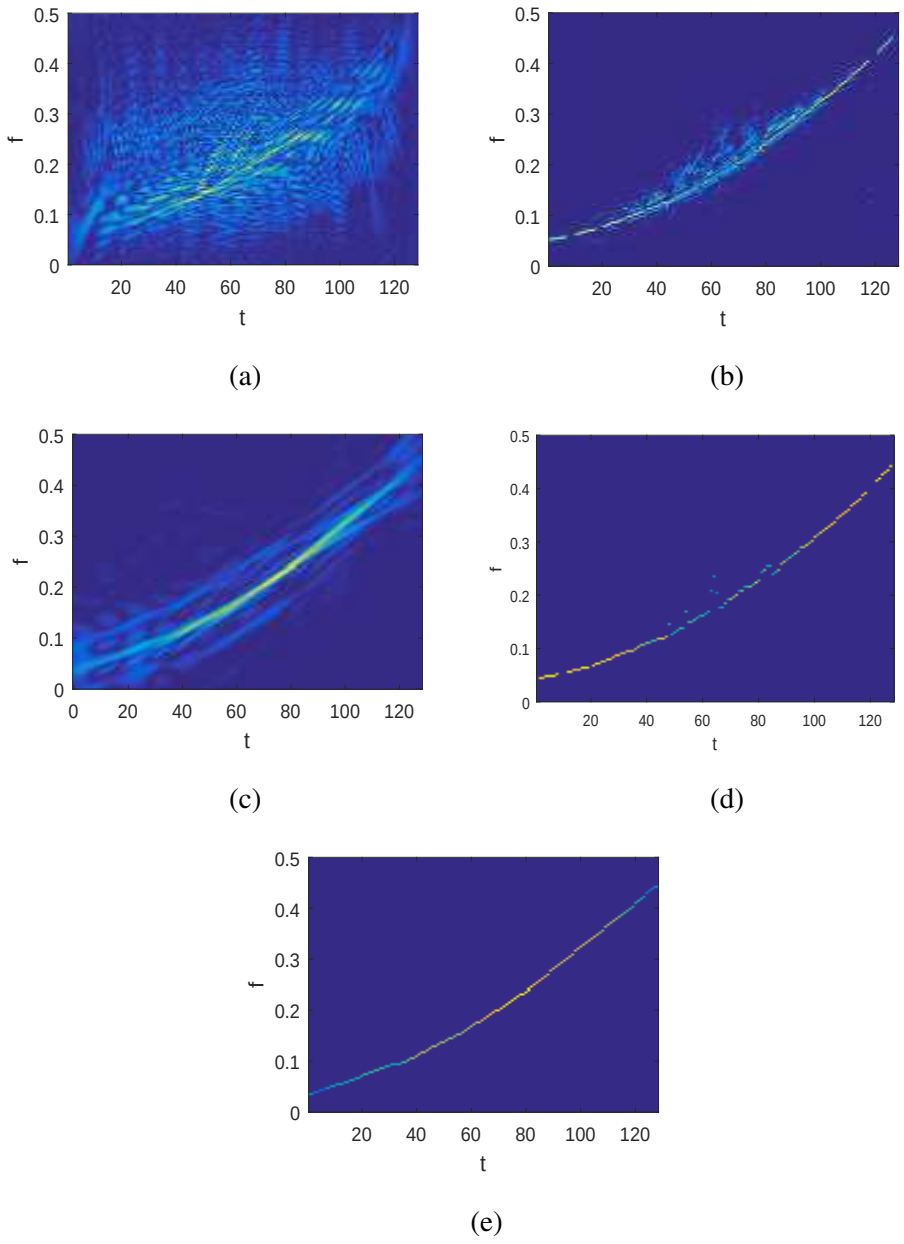

Fig. 9 Scenario 4: Comparison of TFRs obtained using different approaches, applied to the received signal depicted in Fig. 5(a), where the 48 missing samples are clustered into 6 bursts, each containing different numbers of missing samples. (a) MIAA applied to the time domain data; (b) MIAA applied to the IAF; (c) AOK; (d) MI-SR; (e) MI-SR applied to the kerneled IAF.

complexity.

B. Comparison of RMSE of TFRs

In order to quantitatively compare the fidelity of the reconstructed TFRs provided in Section V-A, we first present the RMSE performance of the normalized frequencies, obtained in the noise-free case, in Table 1. It is observed that the results of both MI-SR approaches, obtained respectively from the unkerneled and kerneled IAFs of the received signals, yield low RMSE values. To further examine the performance in the presence of noise, we provide the RMSE performance in Figs. 10(a)–10(d) in the presence of different levels of complex white Gaussian noise for the missing data patterns respectively described in Figs. 2(a), 3(a), 4(a), and 5(a). The RMSE obtained for each SNR is averaged over 50 independent trials. As seen from Fig. 10, the proposed MI-SR approaches applied to the unkerneled and the kerneled IAFs perform better than the WVD, MIAA and AOK based approaches for all the SNR values being considered. For lower SNR values, the MI-SR applied to the kerneled IAF performs slightly better than that applied to the unkerneled IAF because of the cross-term suppression capability of the adaptive TF kernels. However, for high SNR values, the MI-SR approaches exploiting unkerneled and kerneled IAFs yield comparable RMSE results.

Table 1 RMSE of the TFRs shown in Figs. 6–9

	RMSE			
	Scenario 1	Scenario 2	Scenario 3	Scenario 4
WVD	0.0852	0.0871	0.0874	0.0894
MIAA (to data)	0.0757	0.0675	0.0790	0.0754
MIAA (to IAF)	0.0619	0.0767	0.0798	0.0720
AOK	0.0542	0.0542	0.0552	0.0537
MI-SR	0.0520	0.0525	0.0546	0.0515
MI-SR (to kerneled IAF)	0.0517	0.0522	0.0535	0.0518

C. Comparison of Energy Concentrations of TFRs

One of the important performance measure of the TFR reconstruction technique is its ability to preserve high energy concentration of the signal auto-terms and suppress undesired cross-terms. We quantitatively compare the performance of the proposed MI-SR technique with other aforementioned approaches in terms of their TFR energy concentration, as described in [54], [55]. First, we normalize the TFR matrix, $\mathbf{X}$, such that $\sum_{t=1}^{T}\sum_{p=1}^{P}|\rho(t,p)| = 1$. Then, their energy concentration measure, $\xi[\mathbf{X}]$, is computed

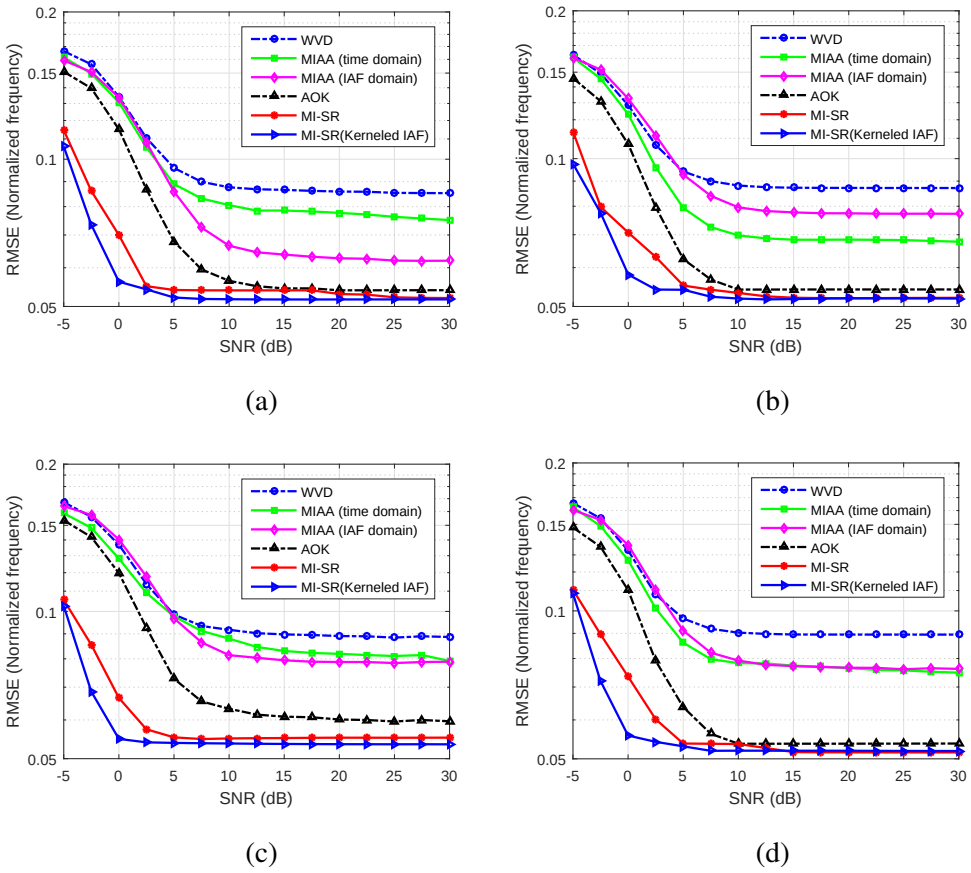

Fig. 10 Comparison of the RMSE of different approaches in the presence of complex white Gaussian noise for the burst missing sample patterns used in (a) Fig. 2; (b) Fig. 3; (c) Fig. 4; (d) Fig. 5.

as [55]

$$\xi[\mathbf{X}] = \left(\sum_{t=1}^{T} \sum_{p=1}^{P} |\rho(t,p)|^{\frac{1}{q}} \right)^{q}, \tag{34}$$

where $q > 1$. TFRs with high energy concentration yield lower values of $\xi[\mathbf{X}]$. The energy concentration measures of all TFRs shown in Figs. 6–9 are summarized in Table 2, for the case of $q = 2$. The proposed MI-SR techniques applied to the unkerneled and kerneled IAFs of the received signal respectively yield the lowest and the second lowest values of the energy measures, indicating their highest energy concentration among all the TFRs being compared. These results confirm our observations in Section V-A.

Table 2 Comparison of energy concentrations of the TFRs

	Scenario 1	Scenario 2	Scenario 3	Scenario 4
WVD	11,916.9	10,782.0	12,297.2	11,598.8
MIAA (to data)	11,723.7	11,143.7	11,817.1	11,855.8
MIAA (to IAF)	1,883.1	1,569.3	2,013.5	1,788.7
AOK	7,842.0	6,167.1	7,334.7	7,967.3
MI-SR	119.2	117.4	120.0	115.9
MI-SR (to kerneled IAF)	123.5	122.3	126.2	124.2

D. Effects of Percentage of the Burst Missing Samples

We examine the effects of the percentage of burst missing samples on the TFR reconstruction performance of the considered approaches. The same signal defined in (21) is considered. The SNR is considered to be 15 dB and each missing data burst contains 10 missing samples. The missing data bursts are assumed to be mutually non-overlapping. We start from 1 missing data burst at a time and gradually increases the total number of missing data bursts to 10. Thus, the total number of missing data samples varies from 10 to 100. Given $T = 128$, they respectively amount to 7.81, 15.63, 23.44, 31.25, 39.06, 46.88, 54.69, 62.50, 70.31 and 78.10 percentage of the total samples. The RMSE is obtained by averaging over 50 trials with independent noise realizations.

We consider two cases. In the first case, we start from the first missing burst, and one more new missing burst adjacent to the previous burst is added at a time. In this case, the location of the previous bursts remains unchanged. In the second case, missing data bursts are uniformly distributed over time and, hence, the positions of the missing data bursts would differ as the number of missing samples varies.

Fig. 11(a) shows the received signal with the final 10 bursts of missing samples. Figs. 11(b) and 11(c) respectively illustrate the RMSE results related to the two cases. As seen from Figs. 11(b) and 11(c), when the number of burst missing samples is small, the overall RMSE values of the different approaches and the increment in their values relative to the percentage of burst missing samples are lower for the second case as compared to the first case. In both the cases, the RMSE of the proposed MI-SR approach, applied to the unkerneled and the kerneled IAFs, respectively, consistently assume the second lowest and the lowest values for all the percentage of the burst missing samples.

E. Performance Comparison for Multi-component FM Signal

In this example, we consider TFR reconstruction of multi-component non-linear FM signals. For illustration purposes, we use a two-component FM signal, and the instantaneous phase laws of the two

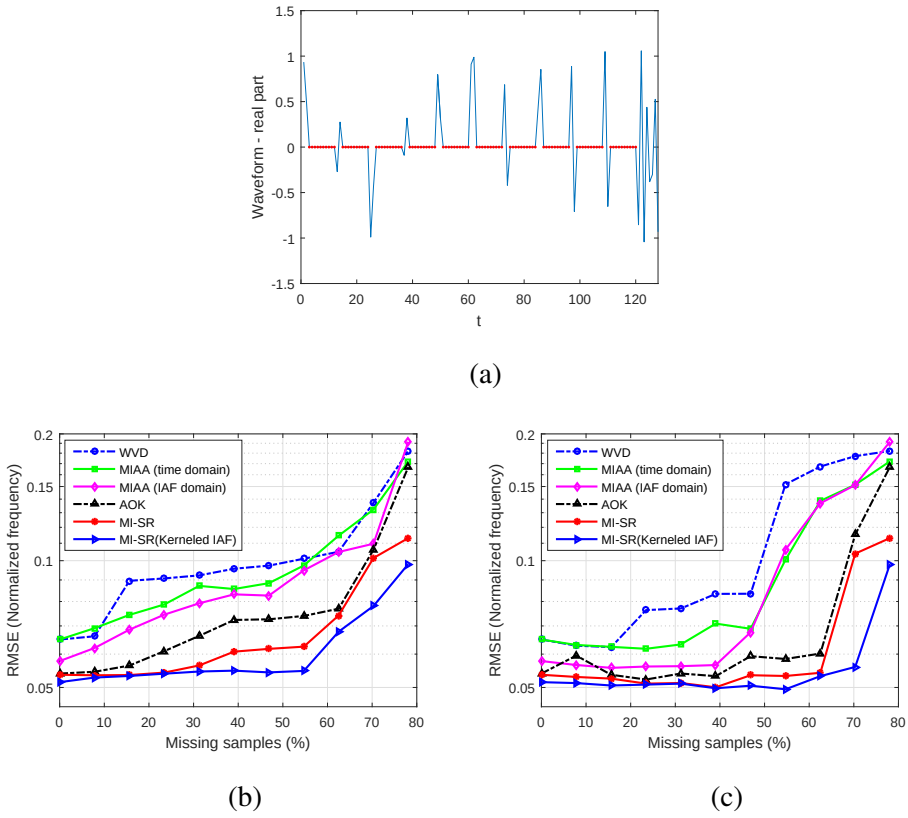

Fig. 11 (a) The real-part waveform of the received signal with final 10 bursts of missing samples, each burst having 10 samples; (b) The RMSE for Case 1; (c) The RMSE for Case 2.

components are given by,

$$\begin{aligned}\phi_1(t) &= 0.05t + 0.05t^2/T + 0.1t^3/T^2,\\ \phi_2(t) &= 0.15t + 0.05t^2/T + 0.1t^3/T^2,\end{aligned} \tag{35}$$

where $t = 1, ..., T$, with T being selected as 128. In order to clearly demonstrate the effects of burst missing samples on the TFR recovery performance, we only consider the noise-free case.

Fig. 12(a) shows the real-part of the original signal waveform without missing samples, and Fig. 12(b) shows that of the received signal with the same burst missing pattern used in Fig. 5. Fig. 13 presents the TFRs obtained using different approaches applied to the received signal depicted in Fig. 12(b). These results are comparable to those demonstrated in Figs. 6 and 9. Clearly, both the WVD in Fig. 13(a) and the MIAA applied to the time-domain data in Fig. 13(b) fail to obtain clear IFs. The Fig. 13(c) shows the TFR, obtained by applying the MIAA to the IAF, with excessive cross-terms and blurring. The AOK effectively suppresses the cross-terms, but the aliasing and artifacts along the frequency axis remain an issue, as depicted in Fig. 13(d). Fig. 13(e) shows the MI-SR result, which outperforms the MIAA and

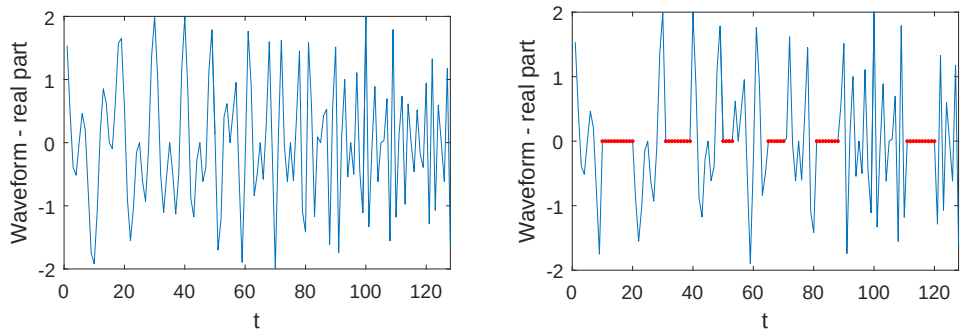

(a) (b)

Fig. 12 Real part of the two-component non-linear FM signal: (a) The original signal; (b) The received signal with burst missing sample pattern used in Fig. 5.

the AOK in both suppressing the artifacts due to burst missing samples and removing aliasing. However, as mentioned earlier, the MI-SR alone does not effectively suppress all cross-terms. As a result, in the underlying case of the multi-component non-linear FM signal, cross-terms between two signal components are still clearly observed. Such drawback can be overcome to achieve resilient TFR reconstruction by applying the MI-SR to the kerneled IAF. Fig. 13(f) shows such a robust TFR result with consistent and clear IF estimates, after effective suppression of the undesired effects of the cross-terms and artifacts by applying MI-SR to the kerneled IAF.

F. Comparison of Execution Time

The executive time is compared for the single-component FM signal described in Section V-A. We first compare the required execution time for each of the aforementioned methods averaged over 50 independent trials to produce results shown in Fig. 6. The average execution times obtained from the 50 independent trials are 0.65, 16.65, 1.20, 0.10, and 1.30 seconds, respectively, for the MIAA applied to the time domain data, the MIAA applied to the IAF, the AOK, the MI-SR, and the MI-SR applied to the kerneled IAF. Similar observations are made for the other scenarios as well but are omitted to avoid repetition. We used Matlab 2017b at a desktop computer with Intel Core i7-6700 processor (Quad Core, 3.4 GHz), and the memory size is 16 GB. Note that, as the MIAA applied to the time-domain data does not yield satisfactory TFR reconstruction results, the execution time is listed only for reference. From these results, the execution time of the MI-SR is only about 1/166 of that performing the MIAA to the IAF, and 1/12 of the time to perform AOK-based TFR reconstruction. On the other hand, the time to

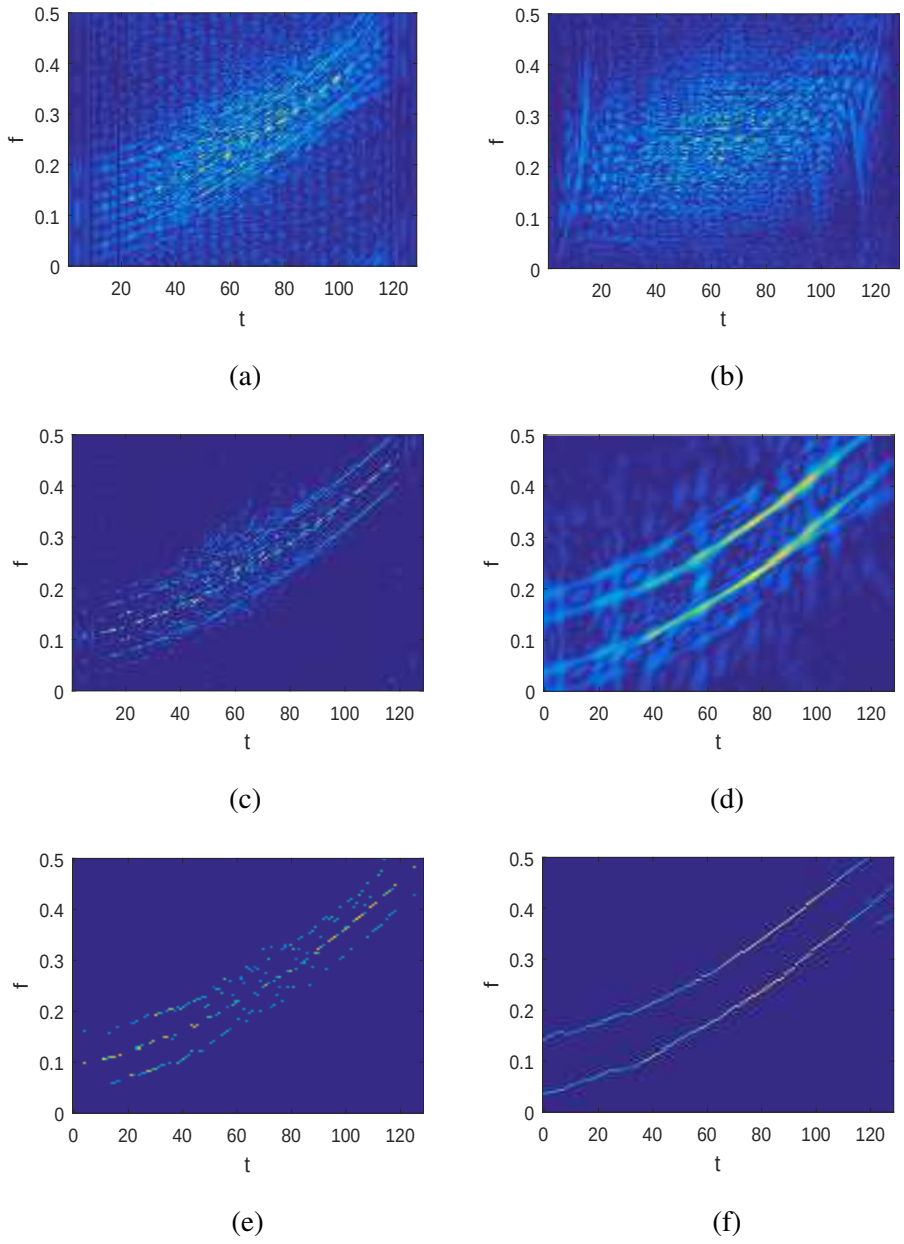

Fig. 13 Comparison of the TFRs of the signal depicted in Fig. 12(b) obtained using different approaches, where the 48 missing samples are clustered into 6 bursts, each containing different numbers of missing samples. (a) WVD; (b) MIAA applied to the time domain data; (c) MIAA applied to the IAF; (d) AOK; (e) MI-SR; (f) MI-SR applied to the kerneled IAF.

execute MI-SR on the kerneled IAF is only about 1/13 of the time required to compute MIAA applied to the IAF.

Next, we compare the required execution time with respect to the number of iterations for the iterative

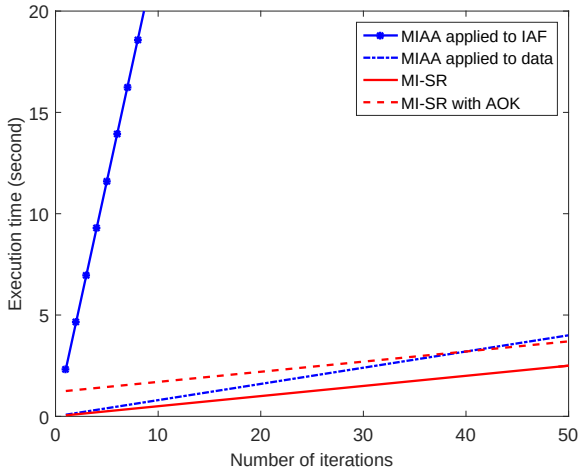

Fig. 14 Comparison of execution time of the MIAA applied to the time domain data, the MIAA applied to the IAF, the MI-SR, and the MI-SR applied with AOK.

approaches, namely, the MI-SR and the MIAA, and the results are summarized in Fig. 14. We observe that, for the same number of iterations, the required execution time of the MIAA, when applied to the time domain data, is slightly higher than that of the MI-SR. However, the difference in the execution time of these two approaches becomes more significant when both are applied to the IAF domain. In addition, such difference in the execution time increases linearly with the number of iterations. For the MI-SR applied with AOK, because the AOK is performed only once, the added execution time does not scale with respect to the number of iterations. As such, the computational complexity of the proposed MI-SR approach, whether executed alone or with the AOK, is much lower than that required to perform MIAA to the IAF.

VI. Conclusions

In this paper, we have provided mathematical analyses of the effects of burst missing data samples in the time-lag domain and on the resulting quadratic TFRs. We have developed a novel MI-SR algorithm to obtain sparsity-based TFRs for non-parametric FM signals in the presence of burst missing samples. The proposed MI-SR method iteratively estimates the TFRs and the missing IAF entries corresponding to the burst missing data until convergence is achieved. The superiority of the proposed approach is examined in terms of the TFR consistency, RMSE, energy concentration and execution time compared with existing techniques based on AOK and MIAA.

REFERENCES

[1] B. Boashash, "Estimating and interpreting the instantaneous frequency of a signal – part 1: Fundamentals," *Proc. IEEE*, vol. 80, no. 4, pp. 520–538, Apr. 1992.

[2] A. Papandreou-Suppappola (Ed.), *Applications in Time-Frequency Signal Processing*. CRC Press, 2002.

[3] V. C. Chen, *The Micro-Doppler Effect in Radar*. Norwood, MA, USA: Artech House, 2011.

[4] D. S. Williamson and D. Wang, "Time-frequency masking in the complex domain for speech dereverberation and denoising," *IEEE/ACM Trans. Audio, Speech, Language Process.*, vol. 25, no. 7, pp. 1492–1501, July 2017.

[5] V. C. Chen and H. Ling, *Time-frequency Transforms for Radar Imaging and Signal Analysis*. Boston, USA: Artech House, 2002.

[6] X-G. Xia, G. Wang, and V. C. Chen, "Quantitative SNR analysis for ISAR imaging using joint time-frequency analysis-Short time Fourier transform," *IEEE Trans. Aerosp. Electron. Syst.*, vol. 38, no. 2, pp. 649–659, Apr. 2002.

[7] H. Zhang, G. Bi, W. Yang, S. Razul, and C. See, "IF estimation of FM signals based on time-frequency image," *IEEE Trans. Aerosp. Electron. Syst.*, vol. 51, no. 1, pp. 326–343, Jan. 2015.

[8] Y. D. Zhang, J. J. Zhang, M. G. Amin, and B. Himed, "Instantaneous altitude estimation of maneuvering targets in over-the-horizon radar exploiting multipath Doppler signatures," *EURASIP J. Adv. Signal Process.*, vol. 2013, no. 2013:100, pp. 1–13, May 2013.

[9] S. Subedi, Y. D. Zhang, M. G. Amin, and B. Himed, "Group sparsity based multi-target tracking in passive multi-static radar systems using Doppler-only measurements," *IEEE Trans. Signal Process.*, vol. 64, no. 14, pp. 3619–3634, July 2016.

[10] L. Cohen, "Time-frequency distributions – A review," *Proc. IEEE*, vol. 77, no. 7, pp. 941–981, July 1989.

[11] B. Boashash, "Estimating and interpreting the instantaneous frequency of a signal – Part 2: Algorithms and applications," *Proc. IEEE*, vol. 80, no. 4, pp. 540–568, Apr. 1992.

[12] P. Flandrin, *Time-Frequency/Time-Scale Analysis*. Academic Press, 1999.

[13] M. Hussain and B. Boashash, "Adaptive instantaneous frequency estimation of multicomponent FM signals using quadratic time-frequency distributions," *IEEE Trans. Signal Process.*, vol. 50, no. 8, pp. 1866–1876, Aug. 2002.

[14] A. Khan and B. Boashash, "Instantaneous frequency estimation of multicomponent nonstationary signals using multiview time-frequency distributions based on the adaptive fractional spectrogram," *IEEE Signal Process. Lett.*, vol. 20, no. 2, pp. 157–160, Feb. 2013.

[15] S. Wang, X. Chen, G. Cai, B. Chen, X. Li, and Z. He, "Matching demodulation transform and synchrosqueezing in time-frequency analysis," *IEEE Trans. Signal Process.*, vol. 62, no. 1, pp. 69–84, Jan. 2013.

[16] B. Boashash (Ed.), *Time-Frequency Signal Analysis and Processing*, 2nd ed. Academic Press, 2016.

[17] Y. Wang, J. Li, and P. Stoica, *Spectral Analysis of Signals: The Missing Data Case*. Morgan and Claypool Publishers, 2006.

[18] Y. D. Zhang, M. G. Amin, and B. Himed, "Reduced interference time-frequency representations and sparse reconstruction of undersampled data," in *Proc. European Signal Process. Conf.*, Marrakech, Morocco, Sept. 2013, pp. 1–5.

[19] Q. Wu, Y. D. Zhang, and M. G. Amin, "Continuous structure based Bayesian compressive sensing for sparse reconstruction of time-frequency distributions," in *Proc. Int. Conf. Digital Signal Process.*, Hong Kong, China, Aug. 2014, pp. 831–836.

[20] B. Jokanovic, M. G. Amin, Y. D. Zhang, and F. Ahmad, "Time-frequency kernel design for sparse joint-variable signal representations," in *Proc. European Signal Process. Conf.*, Lisbon, Portugal, Sept. 2014, pp. 2100–2104.

[21] L. Stankovic, S. Stankovic, I. Orovic, and Y. D. Zhang, "Time-frequency analysis of micro-Doppler signals based on compressive sensing," in *Compressive Sensing for Urban Radars*, M. Amin, Ed. CRC Press, 2014, pp. 283–326.

[22] B. Jokanovic and M. G. Amin, "Reduced interference sparse time-frequency distributions for compressed observations," *IEEE Trans. Signal Process.*, vol. 63, no. 24, pp. 6698–6709, Dec. 2015.

[23] M. G. Amin, B. Jokanovic, Y. D. Zhang, and F. Ahmad, "A sparsity-perspective to quadratic time-frequency distributions," *Digital Signal Process.*, vol. 46, pp. 175–190, Nov. 2015.

[24] E. Sejdic, I. Orovic, and S. Stankovic, "Compressive sensing meets time–frequency: An overview of recent advances in time–frequency processing of sparse signals," *Digital Signal Process.*, vol. 77, pp. 22–35, June 2018.

[25] P. Flandrin and P. Borgnat, "Time-frequency energy distributions meet compressed sensing," *IEEE Trans. Signal Process.*, vol. 58, no. 6, pp. 2974–2982, June 2010.

[26] R. G. Baraniuk and D. L. Jones, "A signal-dependent time-frequency representation: Optimal kernel design," *IEEE Trans. Signal Process.*, vol. 41, no. 4, pp. 1589–1602, Apr. 1993.

[27] D. L. Jones and R. G. Baraniuk, "An adaptive optimal-kernel time-frequency representation," *IEEE Trans. Signal Process.*, vol. 43, no. 10, pp. 2361–2371, Oct. 1995.

[28] N. Khan and B. Boashash, "Multi-component instantaneous frequency estimation using locally adaptive directional time frequency distributions," *Int. J. Adaptive Control Signal Process.*, vol. 30, pp. 429–442, Mar. 2016.

[29] S. S. M. Monfared, A. Taherpour, and T. Khattab, "Time-frequency compressed spectrum sensing in cognitive radios," in *Proc. IEEE GlobeCom*, Atlanta, GA, USA, Dec. 2013, pp. 1088–1094.

[30] B. Jokanovic, M. G. Amin, Y. D. Zhang, and F. Ahmad, "Multi-window time-frequency signature reconstruction from undersampled continuous wave radar measurements for fall detection," *IET Radar, Sonar & Navigation*, vol. 9, no. 2, pp. 173–183, Feb. 2015.

[31] L. Guo, Y. D. Zhang, Q. Wu, and M. G. Amin, "DOA estimation of sparsely sampled nonstationary signals," in *Proc. IEEE China Summit and Int. Conf. Signal and Inform. Process.*, Chengdu, China, July 2015, pp. 300–304.

[32] P. Addesso, M. Longo, S. Marano, V. Matta, L. M. Pinto, and M. Principe, "Sparsifying time-frequency distributions for gravitational wave data analysis," in *Proc. Int. Workshop on Compressed Sens. Theory and its Appl. to Radar, Sonar, and Remote Sens. (CoSeRa)*, Pisa, Italy, June 2015, pp. 154–158.

[33] Y. D. Zhang, B. Wang, and M. G. Amin, "Multi-sensor excision of sparsely sampled nonstationary jammers for GPS receivers," in *Proc. ION GNSS+*, Tampa, FL, USA, Sept. 2015, pp. 3307–3313.

[34] S. Liu, Y. D. Zhang and T. Shan, "Sparsity-based frequency-hopping spectrum estimation with missing samples," in *Proc. IEEE Radar Conf.*, Philadelphia, PA, USA, May 2016.

[35] Y. Nguyen, D. McLernon, and M. Ghogho, "Simplified chirp dictionary for time-frequency signature sparse reconstruction of radar returns," in *Proc. Int. Workshop on Compressed Sens. Theory and its Appl. to Radar, Sonar and Remote Sens. (CoSeRa)*, Aachen, Germany, Sept. 2016, pp. 178–182.

[36] M. G. Amin, D. Borio, Y. D. Zhang, and L. Galleani, "Time-frequency analysis for GNSS: From interference mitigation to system monitoring," *IEEE Signal Process. Mag.*, vol. 34, no. 5, pp. 85–95, Sept. 2017.

[37] N. A. Khan and S. Ali, "Sparsity-aware adaptive directional time–frequency distribution for source localization," *Circuits Syst. Signal Process.*, vol. 37, no. 3, pp. 1223–1242, Mar. 2018.

[38] L. Yang, L. Zhao, S. Zhou, and G. Bi, "Sparsity-driven SAR imaging for highly maneuvering ground target by the combination of time-frequency analysis and parametric Bayesian learning," *IEEE J. Sel. Topics Appl. Earth Observ. in Remote Sens.*, vol. 10, no. 4, pp. 1443–1455, Apr. 2017.

[39] S. Liu, Y. D. Zhang, and T. Shan, "Detection of weak astronomical signals with frequency-hopping interference suppression," *Digital Signal Process.*, vol. 72, pp. 1–8, Jan. 2018.

[40] Y. D. Zhang, "Resilient quadratic time-frequency distribution for FM signals with gapped missing data," in *Proc. IEEE Radar Conf.*, Seattle, WA, USA, May 2017, pp. 1765–1769.

[41] P. Stoica, J. Li, and J. Ling, "Missing data recovery via a nonparametric iterative adaptive approach," *IEEE Signal Process. Lett.*, vol. 16, no. 4, pp. 241–244, Apr. 2009.

[42] J. A. Tropp and A. C. Gilbert, "Signal recovery from random measurements via orthogonal matching pursuit," *IEEE Trans. Inf. Theory*, vol. 53, no. 12, pp. 4655–4666, Dec. 2007.

[43] R. Tibshirani, "Regression shrinkage and selection via the lasso," *J. Roy. Statist. Soc. Series B*, vol. 58, no. 1, pp. 267–288, 1996.

[44] S. Ji, D. Dunson, and L. Carin, "Multi-task compressive sensing," *IEEE Trans. Signal Process.*, vol. 57, no. 1, pp. 92–106, Jan. 2009.

[45] Z. Zhang and B. D. Rao, "Sparse signal recovery with temporally correlated source vector using sparse Bayesian learning," *IEEE J. Sel. Topics Signal Process.*, vol. 5, no. 5, pp. 1–15, 2011.

[46] Q. Wu, Y. D. Zhang, M. G. Amin, and B. Himed, "Complex multitask Bayesian compressive sensing," in *Proc. IEEE Int. Conf. Acoust. Speech, Signal Process. (ICASSP)*, Florence, Italy, May 2014, pp. 3375–3379.

[47] Q. Wu, Y. D. Zhang, M. G. Amin, and B. Himed, "Multi-task Bayesian compressive sensing exploiting intra-task correlation," *IEEE Signal Process. Lett.*, vol. 22, no. 4, pp. 430–434, Apr. 2015.

[48] Y. D. Zhang and M. G. Amin, "Compressive sensing in nonstationary array processing using bilinear transforms," in *Proc. IEEE Sensor Array and Multichannel Signal Process. Workshop (SAM)*, Hoboken, NJ, USA, June 2012, pp. 349–352.

[49] H. I. Choi and W. J. Williams, "Improved time-frequency representation of multicomponent signals using exponential kernels," *IEEE Trans. Acoust., Speech, Signal Process.*, vol. ASSP-37, no. 6, pp. 862–871, June 1989.

[50] Y. Zhao, L. E. Atlas, and R. J. Marks, "The use of cone-shaped kernels for generalized time-frequency representations of nonstationary signals," *IEEE Trans. Acoust. Speech, Signal Process.*, vol. 38, no. 7, pp. 1084–1091, July 1990.

[51] B. Boashash (Ed.), *Time Frequency Signal Analysis and Processing*, 1st ed. Elsevier Science, 2003.

[52] G.-O. Glentis and A. Jakobsson, "Efficient implementation of iterative adaptive approach spectral estimation techniques," *IEEE Trans. Signal Process.*, vol. 59, no. 9, pp. 4154–4167, Sept. 2011.

[53] T. Yardibi, J. Li, P. Stoica, M. Xue, and A. B. Baggeroer, "Source localization and sensing: A nonparametric iterative adaptive approach based on weighted least squares," *IEEE Trans. Aerosp. Electron. Syst.*, vol. 46, no. 1, pp. 425–443, Jan. 2010.

[54] M. Mohammadi, A. A. Pouyan, and N. A. Khan, "A highly adaptive directional time-frequency distribution," *Signal, Image and Video Process.*, vol. 10, no. 7, pp. 1369–1376, Octo. 2016.

[55] L. Stankovic, "A measure of some time-frequency distributions concentration," *Signal Process.*, vol. 81, no. 3, pp. 621–631, Mar. 2001.